Journal of General Physiology

ARTICLE

D-type K^+ current rules the function of electrically coupled neurons in a species-specific fashion

Antonella Dapino[1], Federico Davoine[2], and Sebastian Curti[1]

Electrical synapses supported by gap junctions are known to form networks of electrically coupled neurons in many regions of the mammalian brain, where they play relevant functional roles. Yet, how electrical coupling supports sophisticated network operations and the contribution of the intrinsic electrophysiological properties of neurons to these operations remain incompletely understood. Here, a comparative analysis of electrically coupled mesencephalic trigeminal (MesV) neurons uncovered remarkable difference in the operation of these networks in highly related species. While spiking of MesV neurons might support the recruitment of coupled cells in rats, this rarely occurs in mice. Using whole-cell recordings, we determined that the higher efficacy in postsynaptic recruitment in rat's MesV neurons does not result from coupling strength of larger magnitude, but instead from the higher excitability of coupled neurons. Consistently, MesV neurons from rats present a lower rheobase, more hyperpolarized threshold, as well as a higher ability to generate repetitive discharges, in comparison to their counterparts from mice. This difference in neuronal excitability results from a significantly higher magnitude of the D-type K^+ current (ID) in MesV neurons from mice, indicating that the magnitude of this current gates the recruitment of postsynaptic-coupled neurons. Since MesV neurons are primary afferents critically involved in the organization of orofacial behaviors, activation of a coupled partner could support lateral excitation, which by amplifying sensory inputs may significantly contribute to information processing and the organization of motor outputs.

Introduction

Electrical synaptic transmission is a modality of communication mediated by gap junctions, which represent areas of close apposition between the plasmatic membrane of neurons characterized by the presence of clusters of intercellular channels (Bennett, 1997). These junctions establish pathways of low resistance for the flow of ionic currents supporting the bidirectional and fast communication of both depolarizing and hyperpolarizing signals between neurons (Connors and Long, 2004; Bennett and Zukin, 2004; Pereda et al., 2013). These characteristics allow electrical synapses to contribute to relevant functional operations by neural circuits in many brain areas. Among these operations, lateral excitation results from the ability of electrical coupling to spread excitation within neural circuits, thus creating functional compartments. In this way, the activity in some cells promotes the activation of neighboring coupled ones, thus, operating as a network-boosting mechanism. Although this operation might degrade spatial specificity within neural circuits, lateral excitation between primary afferents tuned to qualitatively similar stimuli acts to boost sensory responses involved in the organization of motor outputs as was shown in invertebrates and lower vertebrates (El Manira et al., 1993; Pereda et al., 1995; Herberholz et al., 2002; Antonsen et al., 2005; Curti et al., 2022). In mammals, this mechanism has also been implicated in the enhancement of excitability in circuits of electrically coupled neurons of the olfactory bulb (Christie and Westbrook, 2006), the cerebellum (Vervaeke et al., 2012), and the dorsal cochlear nucleus (Apostolides and Trussell, 2013, 2014). Moreover, in the retina, lateral excitation provides a mechanism for the precise detection of the spatial location of a moving stimulus, disregarding its velocity (Trenholm et al., 2013).

Mesencephalic trigeminal (MesV) neurons are a special class of primary afferents, whose cell bodies, instead of being located in peripheral ganglia, are distributed in the brainstem (Weinberg, 1928). The peripheral branches of these pseudo-unipolar neurons innervate the spindles of jaw-closing muscles

---

[1]Laboratorio de Neurofisiología Celular, Departamento de Fisiología, Facultad de Medicina, Universidad de la República, Montevideo, Uruguay; [2]Instituto de Ingeniería Eléctrica, Facultad de Ingeniería, Universidad de la República, Montevideo, Uruguay.

Correspondence to Sebastian Curti: scurti@fmed.edu.uy

A preprint of this paper was posted on bioRxiv on January 6, 2023. This work is part of a special issue on the Structure and Function of Ion Channels in Native Cells and Macromolecular Complexes.

and mechanoreceptors of periodontal ligaments, whereas the central processes supply sensory input to neurons of the trigeminal motor nucleus, the rostral parvocellular reticular formation, and the nucleus supratrigeminalis (Dessem and Taylor, 1989; Liem et al., 1991). On the other hand, MesV neurons receive synaptic input at their somata from the hypothalamus and various brainstem structures (Lazarov, 2002; Verdier et al., 2004), supporting the notion that these afferents not only relay peripheral information but are also an integral part of the central circuit involved in the generation of masticatory patterns (Morquette et al., 2012). Previous work in rats and mice has shown that MesV neurons are electrically coupled by means of large connexin36 (Cx36) containing somato-somatic contacts characterized by one to three clusters of multiple Cx36-puncta (Curti et al., 2012; Nagy and Lynn, 2018). Additionally, rather than extensive as observed in most structures of the mammalian brain (Connors and Long, 2004; Bennett and Zukin, 2004), coupling in this nucleus is restricted to pairs or small clusters of neurons (Baker and Llinás, 1971; Curti et al., 2012). Moreover, the dynamic interaction of electrical coupling with their intrinsic electrophysiological properties supports the strong synchronization of pairs of MesV neurons and allows them to operate as coincidence detectors (Curti et al., 2012; Davoine and Curti, 2019).

A previous study based on dye transfer experiments and electrophysiological recordings showed that the incidence of coupling in the MesV nucleus is about three times higher in mice compared with rats (Curti et al., 2012). This contrasting circuital organization in homologous circuits subserving the same function in highly related species is surprising, raising the possibility that electrical contacts also present functional differences between both species. Particularly, we focused on the ability of spikes in active neurons to recruit inactive electrically coupled ones, as it represents a critical aspect for operations like synchronization and lateral excitation. Strikingly, here we show that despite similar coupling strength, recruitment of coupled neurons in rats is dramatically more efficient than in mice. Such difference does not result from dissimilarities of the gap junctions themselves, but instead from the properties of the nonsynaptic membrane of coupled neurons between species. More specifically, by combining electrophysiological and pharmacological evidence with a comparative approach, we show that the observed interspecific difference results from a significantly higher functional expression of the D-type K^+ current in MesV neurons from mice. These results identify a role for the subthreshold K^+ currents in determining the efficacy of postsynaptic recruitment at electrical synapses, and hence the mode of operation of networks of coupled neurons. This emphasizes the role of voltage-dependent membrane conductances in circuits of electrically coupled neurons and its possible contribution to the early stages of sensory processing by primary afferents involved in the organization of relevant behaviors.

Materials and methods

Ethical approval

Sprague-Dawley rats (age: P7–P16) and C57BL mice of either sex (age: P12–P18) were obtained from the university animal facility accredited by the local authorities (CHEA: Comisión Honoraria de Experimentación Animal of Universidad de la República, Uruguay). All animal care and experimental procedures were performed in accordance with national guidelines and laws, with a minimization of the number of animals used. Protocols were approved by the CNEA (Comisión Nacional de Experimentación Animal) and the School of Medicine CEUA (Comisión de Ética en el Uso de Animales, protocols nos. 070153-000128-20 and 070153-000396-17).

Slice preparation and electrophysiology

Animals were decapitated without anesthesia and the brains were quickly removed. Transverse brainstem slices (180–250 µm thick) were prepared using a vibratome (Leica VT 1000s or DSK DTK-1000) in cold sucrose solution containing 248 mM sucrose, 26 mM $NaHCO_3$, 10 mM glucose, 2 mM $MgSO_4$, 2.69 mM KCl, 1.25 mM KH2PO$_4$, and 1 mM $CaCl_2$ for rats, and 213 mM sucrose, 26 mM $NaHCO_3$, 10 mM glucose, 2 mM $MgSO_4$, 2.69 mM KCl, 1.25 mM NaH_2PO_4, 1 mM $CaCl_2$, 0.35 mM ascorbic acid, and 0.3 mM pyruvic acid for mice. In both cases, solutions were bubbled with 95% O_2 and 5% CO_2 (pH ∼7.4). The slices were then transferred to an incubation chamber filled with a physiological solution containing 124 mM NaCl, 2.69 mM KCl, 1.25 mM KH_2PO_4, 26 mM $NaHCO_3$, 10 mM glucose, 2 mM $CaCl_2$, and 2 mM $MgSO_4$ bubbled with 95% O_2 and 5% CO_2 (pH ∼7.4) at 34°C for 30 min. Afterward, the slices were kept at room temperature in the physiological solution until they were transferred into the recording chamber. The recording chamber, mounted on an upright microscope stage (E600; Nikon Eclipse), was continuously perfused with physiological solution (1–1.5 ml/min) at room temperature. Whole-cell patch recordings were performed under visual control using infrared differential interference contrast optics (IR-DIC). MesV neurons were identified on the basis of their location, large spherical somata, and characteristic electrophysiological properties in response to both depolarizing and hyperpolarizing current pulses (Curti et al., 2012). Recording pipettes pulled from borosilicate glass (4–8 MΩ) were filled with intracellular solution containing 148 mM K-gluconate, 3 mM $MgCl_2$, 0.2 mM EGTA, 4 mM Na2-ATP, 0.3 mM Na-GTP, and 10 mM HEPES (pH ∼7.2). The seal resistance between the electrode tip and the cell membrane was higher than 1 GΩ and pipette capacitance was compensated before breaking the seal. Simultaneous recordings from pairs of MesV neurons whose cell bodies lie in close apposition were made using a Multiclamp 700B amplifier (Molecular Devices). Under the current clamp configuration, the voltage drop across the microelectrode resistance was eliminated by means of the bridge balance control of the amplifier. In voltage-clamp configuration, the membrane capacitance and series resistance were compensated (80%) and continuously monitored. Membrane capacitance was obtained from the readout provided by the Multiclamp 700B amplifier during this procedure. Only cells displaying resting membrane potential more negative than −50 mV or spike amplitude above 70 mV for rats or 60 mV for mice were included in this study. Recordings were low-pass filtered at 5 kHz and acquired by means of an analog-to-digital converter connected to a computer, sampled at 10–40 kHz depending on the experiment.

Calculation of coupling coefficient (CC)

During simultaneous whole-cell recordings of pairs of coupled MesV neurons in current clamp, a series of hyperpolarizing current pulses of different amplitudes (−50 to −450 pA) were applied to one cell, whereas the voltage changes were recorded in the same injected neuron (presynaptic, Vpre) and in the coupled one (postsynaptic, Vpost). Plots of Vpost as a function of Vpre (measured at the peak of hyperpolarizing responses, vertical dashed lines in Fig. 2, A and B) were constructed and CC was estimated from the slope of linear regressions. CC values estimated by this method are reported as directions (two directions per coupled pair).

Calculation of the input resistance (Rin)

During simultaneous whole-cell recordings of pairs of coupled MesV neurons in current clamp, a series of hyperpolarizing current pulses of different amplitudes (−50 to −450 pA) were alternatively applied to one or the other cell, whereas the voltage changes were recorded in the same injected neuron (Vm). Plots of Vm as a function of the intensity of injected current were constructed and the Rin was estimated from the slope of linear regressions. This value represents the equivalent resistance of two parallel branches, one corresponding to the non-junctional resistance of the injected neuron and the other to the gap junction plus the non-junctional resistance of the coupled neuron (Bennett, 1966).

Estimation of gap junction conductance

From current clamp recordings, the conductance of electrical contacts (Gj) was estimated as the reciprocal of the resistance (Rj), calculated according to the following equation (Bennett, 1966):

$$Rj = \frac{Rin_{pre} \times Rin_{post} - Rt^2}{Rt},$$

where Rin_{pre} and Rin_{post} are the Rin of the pre- and postsynaptic cells, respectively, and Rt is the transfer resistance defined as the voltage response amplitude in the coupled postsynaptic cell divided by the current amplitude intensity injected in the presynaptic cell. Conductance values estimated by this method are reported as directions (two directions per coupled pair).

Frequency–transfer analysis

The transfer properties between pairs of electrically coupled MesV neurons were determined by injecting frequency-modulated (2–600 Hz or 0.5–100 Hz) sine waves of current into one of the coupled cells (ZAP protocol) while recording the resulting membrane voltage deflections in both cells (see Fig. 4 A, inset). Peak-to-peak intensity (50–300 pA) was adjusted to induce subthreshold voltage deflections. The magnitude of fast Fourier transform (FFT) was calculated for presynaptic and postsynaptic membrane responses, and the frequency–transfer property was determined as the ratio of the postsynaptic FFT magnitude over the presynaptic FFT magnitude. The population frequency–transfer function for both species was determined by averaging single transfers in each recorded direction. Average transfer functions were low-pass filtered by applying a smoothing algorithm and expressed in decibels (dB). The apparent cutoff frequency was determined as the intersection of the slope of the attenuation observed at high frequencies and a horizontal line representing the value observed in DC.

Assessment of MesV neurons excitability

During current clamp recordings, a series of depolarizing current pulses of 200 ms in duration were applied, whose intensities ranged from 50 to 600 pA, in steps of 50 pA. From these recordings, curves of the number of spikes versus current intensity were constructed and the firing gain, defined as the slope of linear regressions forced through the origin, was determined. This parameter reflects the ability of the neuron to produce repetitive discharges as well as its rheobase (minimal current for eliciting firing), representing a valuable indicator of neuronal excitability (Davoine and Curti, 2019).

Recording K^+ currents (IA and ID)

To reduce current intensity through voltage-gated Na^+ channels and HCN channels, NaCl was substituted by choline-Cl, and TTX (0.25 µM) and CsCl (2.5 mM) were added to the physiological solution. In this condition (control), a series of step-like voltage commands of 500 ms in duration, from 0 to 70 mV in steps of 5 mV starting from a holding potential of −70 mV, was simultaneously applied to both recorded neurons. These voltage commands were repeated after the addition of 4-aminopyridine (4-AP) 30 µM and of 4-AP 1 mM. The ID was isolated by subtracting current traces obtained after the addition of 4-AP (30 µM) from those obtained in control, whereas the IA was isolated by subtracting current traces obtained after the addition of 4-AP (1 mM) from those obtained in the presence of 4-AP (30 µM; Storm, 1988; Mitterdorfer and Bean, 2002). From current traces obtained following this procedure, peak values within the first 50 ms of voltage commands were determined and transformed to conductance values by dividing by the corresponding driving force for K^+ to construct activation curves for the ID and the IA. For the construction of inactivation curves, conductance values were determined from maximum currents evoked by 10 ms voltage steps to −30 mV, preceded by voltage commands of 500 ms in duration, from −70 to 0 mV in steps of 5 mV. Activation and inactivation curves were fitted to a Boltzmann equation of the form

$$g(Vm) = \frac{gmax}{1 + e^{\left(\frac{Vhalf - Vm}{slope}\right)}}.$$

From these fits, maximum conductance (gmax), half activation voltage (Vhalf), and slope at Vhalf were obtained. To avoid bias by the difference in cell size, gmax was also reported normalized by the cell's membrane capacitance. The IA and ID half activation voltages were significantly different both in rats (IA Vhalf: −27.9 ± 4.4 mV [SD], $n = 17$; ID Vhalf: −39.2 ± 3.8 mV [SD], $n = 20$; $P = 1.42 \times 10^{-9}$) and mice (IA Vhalf: −28.9 ± 5.2 mV [SD], $n = 14$; ID Vhalf: −36.3 ± 4.2 mV [SD], $n = 13$; P = 0.0004), indicating that these currents were successfully separated following the procedure described above.

Recording of the persistent Na^+ current (INap)

To isolate the INap, currents through K^+ channels and HCN channels were reduced by adding a combination of blockers to the extracellular solution (10 mM TEA-Cl, 1 mM 4-AP, and 5 mM CsCl). In this condition (control), a series of step-like voltage commands of 500 ms in duration, from 0 to 70 mV in steps of 5 mV, starting from a holding potential of −70 mV, were simultaneously applied to both recorded neurons. These voltage commands were repeated after the addition of TTX (0.5 μM). Current traces obtained in TTX were subtracted from those obtained in control, and current intensity was measured after 100 ms of the initiation of the voltage commands. To construct steady-state activation curves, current values were transformed to conductance by dividing by the calculated driving force for Na^+, and the parameters characterizing this process (gmax, Vhalf, and slope at Vhalf) were determined following the same procedure described for the study of K^+ currents.

As no obvious difference in cellular excitability was observed between coupled and uncoupled neurons from both species, Na^+ and K^+ membrane currents were recorded in coupled and uncoupled neurons, and data were pooled. However, in the case of coupled neurons, voltage commands were always simultaneously delivered to both neurons to improve the space clamp.

Data analysis and statistics

Data were analyzed using the following software: Axograph X, Igor Pro7 (Wave Metrics), and Python scientific development environment Spyder (libraries: Numpy, Scipy, Axographio, Stfio, Pandas, and Matplotlib). Results were expressed as average value ± standard deviation (SD). The significance of quantitative data was determined by using Student's *t* test of Igor Pro7 (Wave Metrics). To avoid problems related to pseudoreplication when comparing data from rats and mice (which typically involved recordings obtained in multiple cells from the same animal), two different approaches were adopted (Eisner, 2021). First, for the large data sets presented in Figs. 1, 2, 3, 4, 5, and 9, additional analysis was performed by averaging data values obtained from the same animal and running standard Student's *t* test (Table S1). For smaller data sets presented in Figs. 6 and 7, additional hierarchical analysis was performed by using GraphPad Prism 9, which considers the structure of the data (number of cells per animal), and results are presented in corresponding supplementary figures. All data for the conclusions of this study are reported in the article.

Online supplemental material

Fig. S1 and Fig. S2 show the results of statistical hierarchical analysis (nested Student's *t* test) for data shown in Figs. 6 and 7, respectively. Fig. S3 characterizes the persistent Na^+ current of MesV neurons in both rats and mice, along with the corresponding statistical hierarchical analysis. Fig. S4 displays the contribution of ID to the RMP and Rin in mouse MesV neurons. Table S1 summarizes results from statistical analysis (Student's *t* test) for data sets presented in Figs. 1, 2, 3, 4, 5, and 9, in which data from the same animal was averaged.

Results

Previous work had shown that the incidence of electrical coupling among MesV neurons from rats and mice is dramatically different. Both electrophysiological and tracer coupling experiments revealed that coupling incidence in rats is about 21–23%, whereas in mice it is considerably more prevalent, about 60–63% (Curti et al., 2012). Such findings suggest contrasting principles of network organization in homolog rodent circuits involved in the organization of orofacial behaviors. To determine if such rat–mouse difference in network organization is accompanied by functional dissimilarities, under identical recording conditions, the properties of electrical synaptic transmission between MesV neurons from these species were systematically compared. Most specifically, the ability of presynaptic spikes to recruit postsynaptic neurons was taken as a readout of functional specializations on the basis of two considerations. First, action potentials triggered in response to sensory stimuli at the periphery most probably constitute the main source for electrical coupling potentials at these primary afferents. Second, relevant functional operations of electrical coupling, like synchronization and lateral excitation, rely on the ability of presynaptic neurons to recruit electrically coupled neighbors (Connors and Long, 2004; Pereda et al., 2013; Connors, 2017; Curti et al., 2022). Thus, the efficacy of postsynaptic recruitment was assessed in pairs of electrically coupled MesV neurons from rats and mice. For this, just-suprathreshold depolarizing current pulses were alternatively injected into each neuron of an electrically coupled pair, whereas the membrane potential was simultaneously monitored in both cells (Fig. 1, A–D). From these experiments, the probability of postsynaptic recruitment was estimated separately for each direction (two directions per pair) as the ratio of the number of postsynaptic spikes over the number of presynaptic ones and represented as a percentage (Fig. 1 E). Strikingly, postsynaptic recruitment is significantly more efficient in rats compared with mice, averaging 43.8 ± 48.5% [SD] ($n = 70$ directions, $N = 31$ animals) and 2.4 ± 15.4% [SD] ($n = 125$ directions, $N = 53$ animals), respectively ($P = 1.09 \times 10^{-9}$, unpaired, two-tailed *t* test; see also Table S1). Moreover, this revealed that rat's MesV neurons drive spiking of its postsynaptic coupled neurons in half of the tested directions (35 out of 70 directions, probability > 0%), consistent with previous work showing strong spiking synchronization in coupled pairs (Curti et al., 2012). In striking contrast, the recruitment of postsynaptic neurons by presynaptic spikes occurs only in 2.4% of tested directions (3 out of 125, probability > 0) in mice (Fig. 1 F), despite the coupling strength of these two populations being matched (see below).

The higher efficacy of presynaptic spikes to drive spiking in postsynaptic coupled MesV neurons from rats compared with mice might result from differences in coupling strength between these two species. To avoid any bias due to such differences, the populations of coupled pairs from rats and mice were matched in terms of their CC. Therefore, coupled pairs from mice with very low CC were not included in this study. Accordingly, the CC determined by a series of hyperpolarizing current pulses (Fig. 2, A and B, see Materials and methods) showed no statistical difference between these two species, averaging 0.44 ± 0.18 [SD]

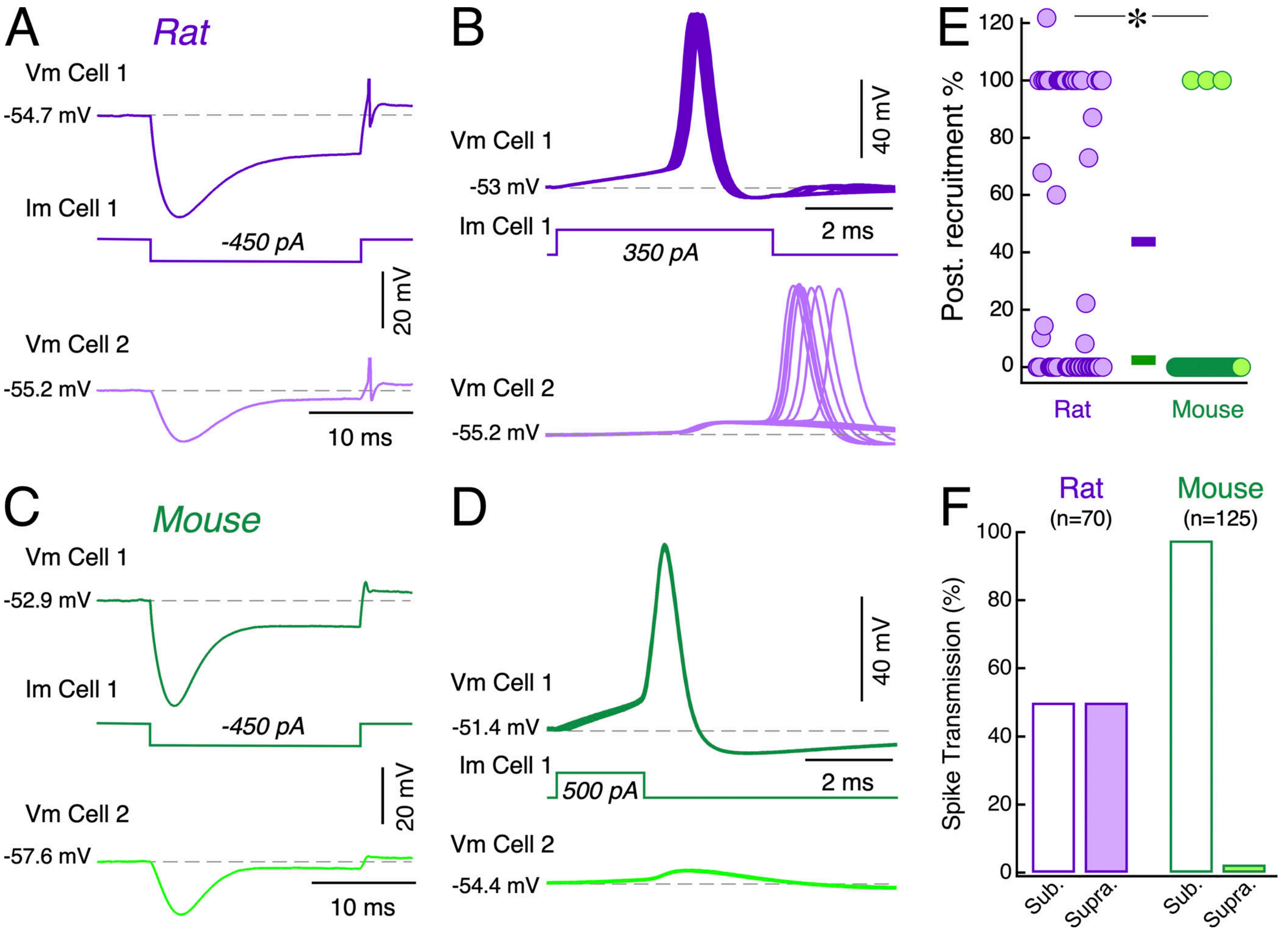

Figure 1. **Postsynaptic recruitment between electrically coupled MesV neurons is considerably more efficient in rats compared with mice. (A and C)** Paired recordings from electrically coupled MesV neurons during the injection of a hyperpolarizing current pulse (Im Cell 1) showing single traces of the voltage membrane response in the injected (Vm Cell 1) and coupled (Vm Cell 2) neurons in rat and mouse, respectively. Values at left of membrane voltage traces denote resting membrane potential in this and subsequent figures. **(B and D)** For the same pairs depicted in A and C, postsynaptic recruitment was assessed by activating the presynaptic neuron with a short depolarizing current pulse (Vm Cell 1) in the rat (B) and mouse (D). Single traces are shown superimposed to estimate the firing probability of the postsynaptic neuron in each species (rat: 57 traces; mouse: 100 traces). **(E)** Plot of the probability of postsynaptic recruitment estimated for each direction as the ratio of the number of postsynaptic spikes over the number of presynaptic ones, and represented as a percentage (rats: 43.8 ± 48.5% [SD], *n* = 70 directions, *N* = 31 animals; mice: 2.4 ± 15.4% [SD], *n* = 125 directions, *N* = 53 animals; P = 1.09 × 10^{-9}, unpaired, two-tailed *t* test). Horizontal bars represent population averages. **(F)** Bar graph illustrating the efficacy of postsynaptic recruitment for the population of coupled pairs, as the fraction of tested directions in which an action potential in one neuron induced firing in the coupled one at least once (probability > 0, Supra.) or not (probability = 0, Sub.) in rats and mice (rat: 70 directions, 35 pairs, 34 animals; mouse: 125 directions, 64 pairs, 55 animals).

(*n* = 70 directions, *N* = 31 animals) and 0.44 ± 0.11 [SD] (*n* = 128 directions, *N* = 53 animals) for rats and mice, respectively (P = 0.981, unpaired, two-tailed *t* test; see also Table S1). Histograms in Fig. 2 C show that CC from mice display a roughly symmetric distribution, while CC from rats is slightly skewed to the right, although this minor difference most probably cannot explain the dramatic dissimilarity in postsynaptic recruitment between these two populations. Consistently, neither of the determinants of the CC, the junctional conductance (Gj), and the Rin of the postsynaptic neuron (Bennett, 1966; Curti and O'Brien, 2016) displayed any statistical difference. The Rin averaged 92.3 ± 25.3 MΩ [SD] (*n* = 70 cells, *N* = 31 animals) and 89.9 ± 27.1 MΩ [SD] (*n* = 128 cells, *N* = 53 animals) in rats and mice, respectively (P = 0.538, unpaired, two-tailed *t* test; see also Table S1; Fig. 2 D), whereas the Gj estimated from current clamp recordings (see Materials and methods), averaged 7.54 ± 5.64 nS [SD] (*n* = 70 directions, *N* = 31 animals) in rats and 6.64 ± 2.56 nS [SD] (*n* = 128 cells, *N* = 53 animals) in mice (P = 0.210, unpaired, two-tailed *t* test; see also Table S1; Fig. 2 E). Also, in the age range employed in this study, neither CC nor Rin showed any correlation with age as indicated by linear regression analysis (rat: CC vs. age slope = 0.011, R^2 = 0.022; mouse: CC vs. age slope = 0.0036, R^2 = 0.0013; rat: Rin vs. age slope = 0.76, R^2 = 0.0047; mouse: Rin vs. age slope = −1.8, R^2 = 0.0057). Moreover, it is worth mentioning that the resting membrane potential of MesV neurons from these two species does not show any statistical difference (rat: −55.6 ± 4.6 mV [SD], *n* = 70 cells, *N* = 31 animals; mouse: −55.3 ± 4.0 mV [SD], *n* = 128 cells, *N* = 50 animals; P = 0.696, unpaired, two-tailed *t* test; see also Table S1; Fig. 2 F). Thus, the disparity in the efficacy of postsynaptic recruitment in rats versus mice

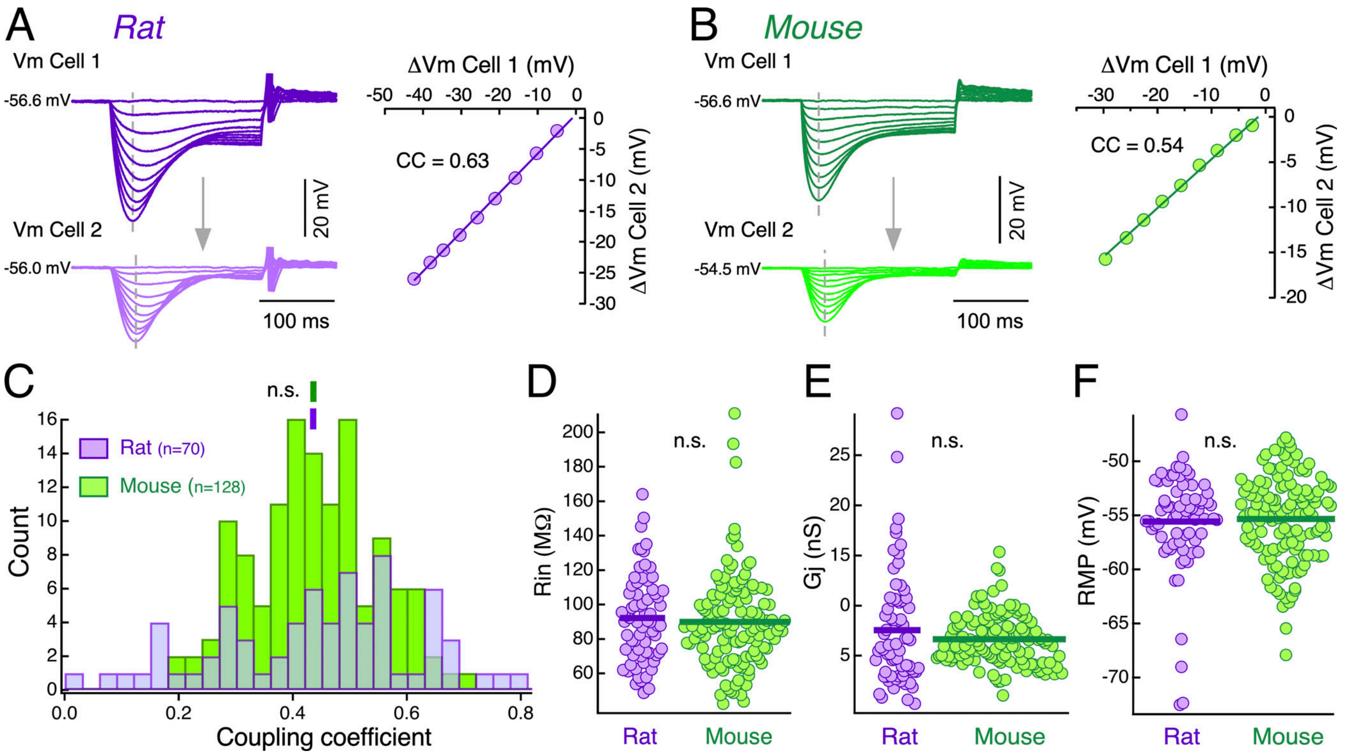

Figure 2. **Characterization of the coupling strength and its determinants. (A and B)** The injection of a series of hyperpolarizing current pulses of increasing intensity into one cell produces corresponding voltage responses in the same cell (Vm Cell 1) and in the coupled cell (Vm Cell 2) in rat (A, left) and mouse (B, left). From these recordings, the CC was estimated by plotting the amplitude of membrane voltage changes (measured at the peak of hyperpolarizing responses, vertical dashed lines) in the postsynaptic cell (Vm Cell 2, ordinates) as a function of membrane voltage changes in the presynaptic cell (Vm Cell 1, abscissas). Each data set was fitted with a straight-line function and the slope values representing the CC are indicated (A and B, right). **(C)** Histogram showing the distribution of CC calculated for the population of recorded directions in rats (purple) and mice (green). Vertical bars above histograms indicate the population average for each data set (rat: 0.44 ± 0.18 [SD], *n* = 70 directions, *N* = 31 animals; mouse: 0.44 ± 0.11 [SD], *n* = 128, *N* = 53 animals; P = 0.981, unpaired, two-tailed *t* test). **(D)** Rin measured in the population of recorded neurons in rats and mice (rat: 92.3 ± 25.3 MΩ [SD], *n* = 70 cells, *N* = 31 animals; mouse: 89.9 ± 27.1 MΩ [SD], *n* = 128 cells, *N* = 53 animals; P = 0.538, unpaired, two-tailed *t* test). **(E)** Gj values estimated in each assessed direction in rats and mice (rat: 7.54 ± 5.64 nS [SD], *n* = 70 directions, *N* = 31 animals; mouse: 6.64 ± 2.56 nS [SD], *n* = 128 directions, *N* = 53 animals; P = 0.210, unpaired, two-tailed *t* test). Horizontal bars in D and E represent population averages. **(F)** Resting membrane potential (RMP) measured in the population of recorded neurons in rats and mice (rat: −55.6 ± 4.6 mV [SD], *n* = 70, *N* = 31 animals; mouse: −55.3 ± 4.0 mV [SD], *n* = 128, *N* = 50 animals; P = 0.696, unpaired, two-tailed *t* test). Horizontal bars in D, E, and F represent population averages.

cannot be explained by a difference in the coupling strength or the resting membrane potential between these species.

Although the CC estimated at the peak of hyperpolarizing voltage responses to current pulses is informative about the coupling strength in the passive regime, it might not faithfully reflect the efficacy of spike transmission. On one hand, transmission at electrical synapses typically behaves as a low-pass filter, meaning that high-frequency signals (like action potentials) are considerably more attenuated in comparison to signals with a lower frequency content. This implies that besides the Gj and the Rin of the postsynaptic cell, the waveform of the presynaptic signal (i.e., its frequency content) also represents a critical determinant of the coupling strength (Bennett, 1966; Connors and Long, 2004; Alcamí and Pereda, 2019; Curti et al., 2022). On the other hand, active subthreshold mechanisms can crucially shape postsynaptic responses. For example, it has been well established that the persistent Na^+ current (INap) is able to significantly increase the efficacy of spike transmission at electrical contacts (Mann-Metzer and Yarom, 1999; Curti and Pereda, 2004; Dugué et al., 2009; Curti et al., 2012).

Thus, to assess the efficacy of spike transmission in rats and mice, spike characteristics were determined first and their impact on the postsynaptic cell was evaluated thereafter. Fig. 3, A and B display representative spikes (top) recorded in MesV neurons from rats and mice, respectively, with their corresponding time derivatives (bottom), illustrating the method employed to measure several spike parameters. While spike duration does not show statistical difference between rats and mice, averaging 0.48 ± 0.14 ms [SD] (*n* = 69 cells, *N* = 31 animals) and 0.50 ± 0.15 ms [SD] (*n* = 117 cells, *N* = 50 animals), respectively (P = 0.316, unpaired, two-tailed *t* test; see also Table S1; Fig. 3 C), spike amplitude is significantly larger in rats (88.7 ± 11.9 mV [SD], *n* = 70 cells, *N* = 31 animals) compared with mice (68.2 ± 12.3 mV [SD], *n* = 118 cells, *N* = 50 animals; $P = 1.29 \times 10^{-21}$, unpaired, two-tailed *t* test; see also Table S1; Fig. 3 D). Moreover, spike after-hyperpolarization (AHP) is also of larger amplitude in rats compared with mice (rat: −5.8 ± 2.5 mV [SD], *n* = 68 cells, *N* = 31 animals; mouse: −4.9 ± 2.1 mV [SD], *n* = 118 cells, *N* = 50 animals; P = 0.019, unpaired, two-tailed *t* test; however, see also Table S1; Fig. 3 E), most probably due to the stronger activation of repolarizing mechanisms during rat action potentials, whose peak levels attain more positive values compared to mice. Thus, although similar in duration, MesV neurons' spikes from rats are on average ~20 mV bigger in amplitude than those from mice. Correspondingly, the maximum value of the spike time derivative is significantly higher in rats versus mice (rat: 310.8 ± 96.6 mV/ms [SD], *n* = 66 cells, *N* = 31 animals; mouse: 183.5 ± 89.6 mV/ms [SD], *n* = 118 cells, *N* = 50 animals; P = 9.3×10^{-15}, unpaired, two-tailed *t* test; see also Table S1), indicating that spikes from rat MesV neurons present a faster time course. Consistently, spike phase plots (first-time derivative of membrane voltage as a function of the membrane voltage) show that trajectories from mice lie almost completely within those of rats' MesV neurons (Fig. 3 F). Also, this analysis revealed that the threshold, defined as the value of membrane voltage at which the rate of change reaches 10 mV/ms, is significantly more hyperpolarized in rats compared with mice (rat: −47.5 ± 5.5 mV [SD], *n* = 66 cells, *N* = 31 animals; mouse: −40.0 ± 5.3 mV [SD], *n* = 118 cells, *N* = 50 animals; P = 4.9×10^{-15}, unpaired, two-tailed *t* test; see also Table S1; Fig. 3 G).

The above result raises the possibility that the higher rate of postsynaptic recruitment in rats might be a consequence of presynaptic spikes larger in amplitude. However, their faster time course, corresponding to larger high-frequency components in the frequency domain, might result in more dramatic attenuation due to the filter properties of electrical synaptic transmission. Consistent with a previous study (Curti et al., 2012), frequency-transfer characteristics determined by ZAP protocols and FFT analysis (see Materials and methods) revealed that despite some degree of frequency preference, electrical transmission between MesV neurons from both species essentially obeys a low-pass filter, with an apparent cutoff frequency of 51 and 40 Hz in rats and mice, respectively (Fig. 4 A). According to these results, predicting the relative efficacy of transmission in these two species is not straightforward as spikes of larger amplitude might result in larger postsynaptic coupling potentials, whereas attenuation of high-frequency components due to low-pass filter properties is expected to have the opposite effect. To directly assess the efficacy of spike transmission in these two species, the spike-related CC (CC Spike) for the population of electrically coupled MesV neurons was compared. For this, the CC Spike was determined as the ratio between the postsynaptic coupling potential (spikelet) amplitude and the amplitude of the presynaptic spike from recordings like those depicted in Fig. 4, B and C. Noteworthy, this analysis revealed that the CC Spike from mice is almost 30% larger than that from rats, averaging 0.094 ± 0.028 [SD] (*n* = 122 directions, *N* = 50 animals) and 0.070 ± 0.034 [SD] (*n* = 57 directions, *N* = 28 animals), respectively (P = 7.66×10^{-6}, unpaired, two-tailed *t* test; see also Table S1; Fig. 4 D), indicating that spike transmission is more efficient in mice compared with rats. This difference most probably results from the fact that spikes from rats seem to present larger high-frequency components in comparison to mice (see above). However, despite this difference in CC Spike, spikelet's amplitudes from these two populations show no statistical difference as they averaged 5.95 ± 2.91 mV [SD] (*n* = 57 cells, *N* = 28 animals) in rats and 6.13 ± 1.41 mV [SD] (*n* = 122 cells, *N* = 50 animals) in mice (P = 0.645, unpaired, two-tailed *t* test; see also Table S1; Fig. 4 E). These results indicate that the higher efficiency of spike transmission in mice is compensated by the lower amplitude of presynaptic spikes, resulting in postsynaptic coupling potentials of similar amplitude.

Preceding results show that in both species presynaptic spikes evoke postsynaptic coupling potentials similar in amplitude, which arise from similar resting membrane potential levels, suggesting that differences in postsynaptic recruitment should result from dissimilarities in membrane excitability. To test this possibility, a detailed characterization of firing properties was performed by using experimental protocols consisting of a series of depolarizing current pulses of increasing intensity (50–600 pA) applied from the cells' RMP (Fig. 5, A and B). From these experiments, plots of the number of spikes as a function of the injected current intensity were constructed (Fig. 5 C). The average behavior of the population of rats and mice can be seen in Fig. 5 D. This graph shows that rat MesV neurons respond with more spikes in almost the entire range of current intensity tested. Consistently, the slope of linear regression to spikes vs. current relationships (firing gain) in rats is significantly higher than in mice, averaging 0.011 ± 0.015 spikes/pA [SD] (range: 0.0004–0.0664, *n* = 70 cells, *N* = 31 animals) and 0.003 ± 0.008 spikes/pA [SD] (range: 0.0004–0.0637, *n* = 99 cells, *N* = 50 animals), respectively (P = 7.19×10^{-5}, unpaired, two-tailed *t* test; see also Table S1; Fig. 5 E), whereas the rheobase for the population of MesV neurons is significantly lower in rats than in mice, averaging 205.7 ± 104.4 pA [SD] (*n* = 70 cells, *N* = 31 animals) and 396.2 ± 181.4 pA [SD] (*n* = 128 cells, *N* = 50 animals), respectively (P = 1.12×10^{-16}, unpaired, two-tailed *t* test; see also Table S1; Fig. 5 F). Noteworthy, in the age range employed in this study, neither firing gain nor rheobase showed any correlation with age as indicated by linear regression analysis (rat: firing gain vs. age slope = 0.001, $R^2 = 0.04$; rheobase vs. age slope = −3.7, $R^2 = 0.007$; mouse: firing gain vs. age slope = 2.1×10^{-5}, $R^2 = 9.9 \times 10^{-6}$; rheobase vs. age slope = 33.3, $R^2 = 0.04$). These results clearly indicate that rat MesV neurons present higher excitability, which is consistent with their lower threshold, and suggest that it might underlie the higher efficacy in postsynaptic recruitment.

To gain insights into the membrane mechanism responsible for such difference in cellular excitability between rats and mice, voltage clamp experiments were designed to characterize the main subthreshold K^+ currents (IA and ID), whose involvement in membrane resonance, oscillations, and bursting has been well established in these neurons (Del Negro and Chandler, 1997; Wu et al., 2001; Enomoto et al., 2006; Saito et al., 2006; Hsiao et al., 2009; Yang et al., 2009). Accordingly, IA and ID of MesV neurons from both species were characterized following standard protocols (see Materials and methods). To avoid bias by the difference in cell size between species, conductance was normalized by the cell's membrane capacitance (density). This is based on the finding that membrane capacitance is on average ~25% larger in rats compared with mice (rats: 55.1 ± 11.4 pF [SD], *n* = 34 cells, *N* = 8 animals; mice: 39.9 ± 10.8 pF [SD], *n* = 36 cells, *N* = 12 animals; P = 2.65×10^{-7}, unpaired, two-tailed *t* test;

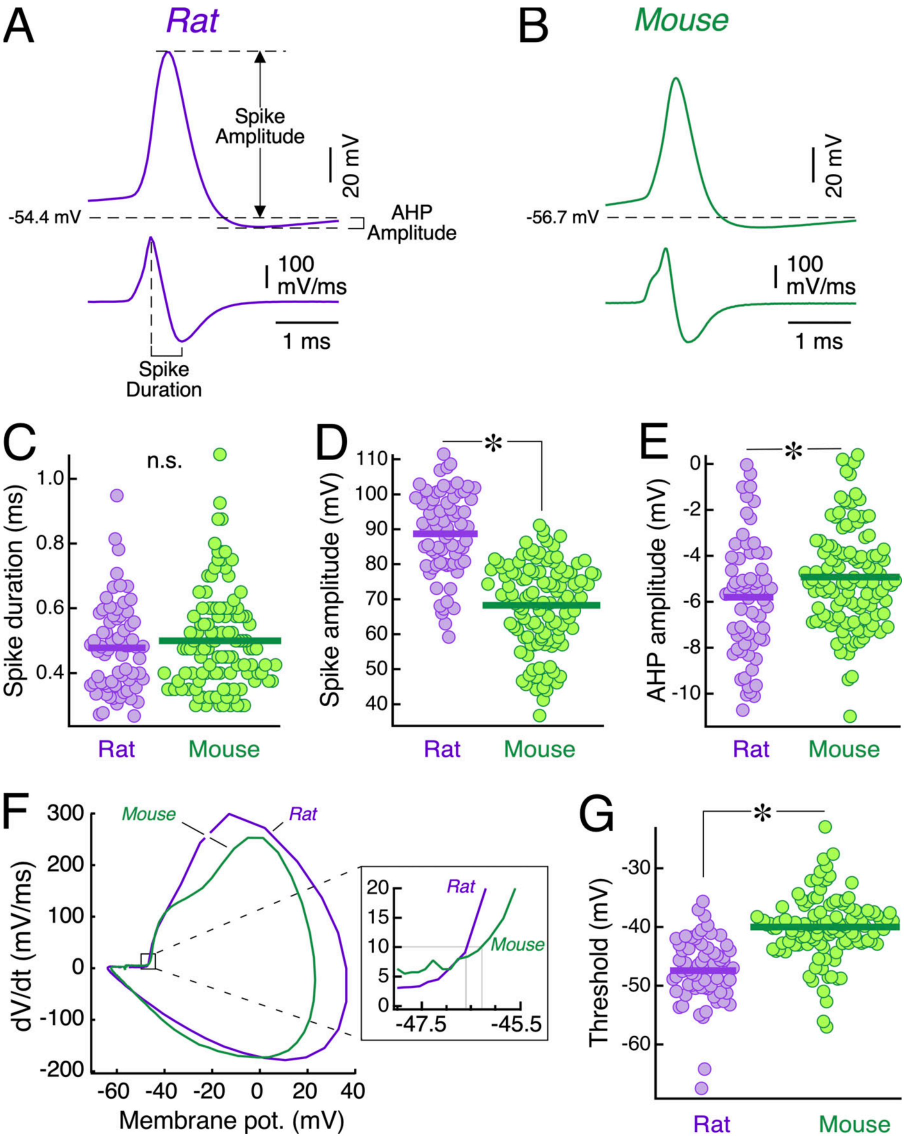

Figure 3. **Spike characteristics of MesV neurons. (A and B)** Representative action potentials from rat and mouse respectively (top), with their corresponding first-time derivative (bottom). Spike and spike AHP amplitudes were measured from resting membrane potential level (RMP) to their peaks, whereas spike duration was measured as the time difference between maximum and minimum values of time derivative. **(C)** Spike duration measured in the population of recorded neurons in rats and mice (rat: 0.48 ± 0.14 ms [SD], *n* = 69 cells, *N* = 31 animals; mouse: 0.50 ± 0.15 ms [SD], *n* = 117 cells, *N* = 50 animals; P = 0.316, unpaired, two-tailed *t* test). **(D)** Spike amplitude measured in the population of recorded neurons in rats and mice (rat: 88.7 ± 11.9 mV [SD], *n* = 70 cells, *N* = 31 animals; mouse: 68.2 ± 12.3 mV [SD], *n* = 118 cells, *N* = 50 animals; P = 1.29 × 10^{-21}, unpaired, two-tailed *t* test). **(E)** AHP amplitude in rats and mice (rat: −5.8 ± 2.5 mV [SD], *n* = 68 cells, *N* = 31 animals; mouse: −4.9 ± 2.1 mV [SD], *n* = 118 cells, *N* = 50 animals; P = 0.019, unpaired, two-tailed *t* test). **(F)** Phase plots of the first-time derivative of the membrane potential (dV/dt) against the instantaneous membrane potential, for the traces depicted in A and B, shown superimposed. Inset: Larger scale of the boxed area in the phase plots. The threshold is indicated for each trace (gray lines). **(G)** Plot of the threshold in rats and mice (rat: −47.5 ± 5.5 mV [SD], *n* = 66, *N* = 31 animals; mouse: −40.0 ± 5.3 mV [SD], *n* = 118, *N* = 50 animals; P = 4.9 × 10^{-15}, unpaired, two-tailed *t* test). Horizontal bars in C, D, E, and G represent population averages.

P = 0.0015, unpaired, two-tailed nested *t* test; data not shown), indicating that MesV neurons from rats present a larger membrane surface area.

Fig. 6 A shows representative results from rats and mice, in which IA was recorded in voltage clamp, during protocols consisting of a series of step commands from 0 to 70 mV in steps of 5 mV and starting from a holding potential of approximately −70 mV. Membrane currents obtained following this procedure showed rapid activation and an inactivation process with kinetics typical of IA (Fig. 6 B; Storm, 1990; Mitterdorfer and Bean, 2002). From membrane current recordings, conductance values were calculated to construct activation curves that were fitted to a Boltzmann function (Fig. 6 C). From these fits, maximum conductance (gmax), half activation voltage (Vhalf), and slope at Vhalf were obtained for the population of recorded neurons. This analysis revealed that IA from rats and mice present similar characteristics and cannot account for differences in membrane excitability between these species. In fact, gmax normalized by the cell's capacitance averaged 1.40 ± 0.61 nS/pF [SD] (*n* = 17 cells, *N* = 5 animals) in rats and 1.42 ± 0.38 nS/pF [SD] (*n* = 14 cells, *N* = 6 animals) in mice (P = 0.944, unpaired, two-tailed *t* test; Fig. 6 D, left), Vhalf averaged −27.9 ± 4.4 mV [SD] (*n* = 17 cells, *N* = 5 animals) in rats and −28.9 ± 5.2 mV [SD] (*n* = 14 cells, *N* = 6 animals) in mice (P = 0.571, unpaired, two-tailed *t* test; Fig. 6 D, middle), whereas slope averaged 9.51 ± 1.71 mV [SD] (*n* = 17 cells, *N* = 5 animals) in rats and 9.55 ± 2.61 mV [SD] (*n* = 14 cells, *N* = 6 animals) in mice (P = 0.969, unpaired, two-tailed *t* test; Fig. 6 D, right). These results were confirmed by hierarchical statistical analysis which considers possible clustering of data obtained from the same animal (Fig. S1).

Representative recordings of ID from rats and mice are shown in Fig. 7 A. This conductance is characterized by its rapid activation and slow voltage-dependent inactivation kinetics (Fig. 7 B). ID inactivation is considerably slower than that of the IA, confirming that they were successfully separated by the experimental protocols. Strikingly, in contrast to the IA, ID gmax is 63% higher in MesV neurons from mice compared with rats, averaging 2.26 ± 0.90 nS/pF [SD] (*n* = 13 cells, *N* = 5 animals) and 1.39 ± 0.56 nS/pF [SD] (*n* = 20 cells, *N* = 5 animals), respectively (P = 0.0057, unpaired, two-tailed *t* test; Fig. 7, C and D, left),

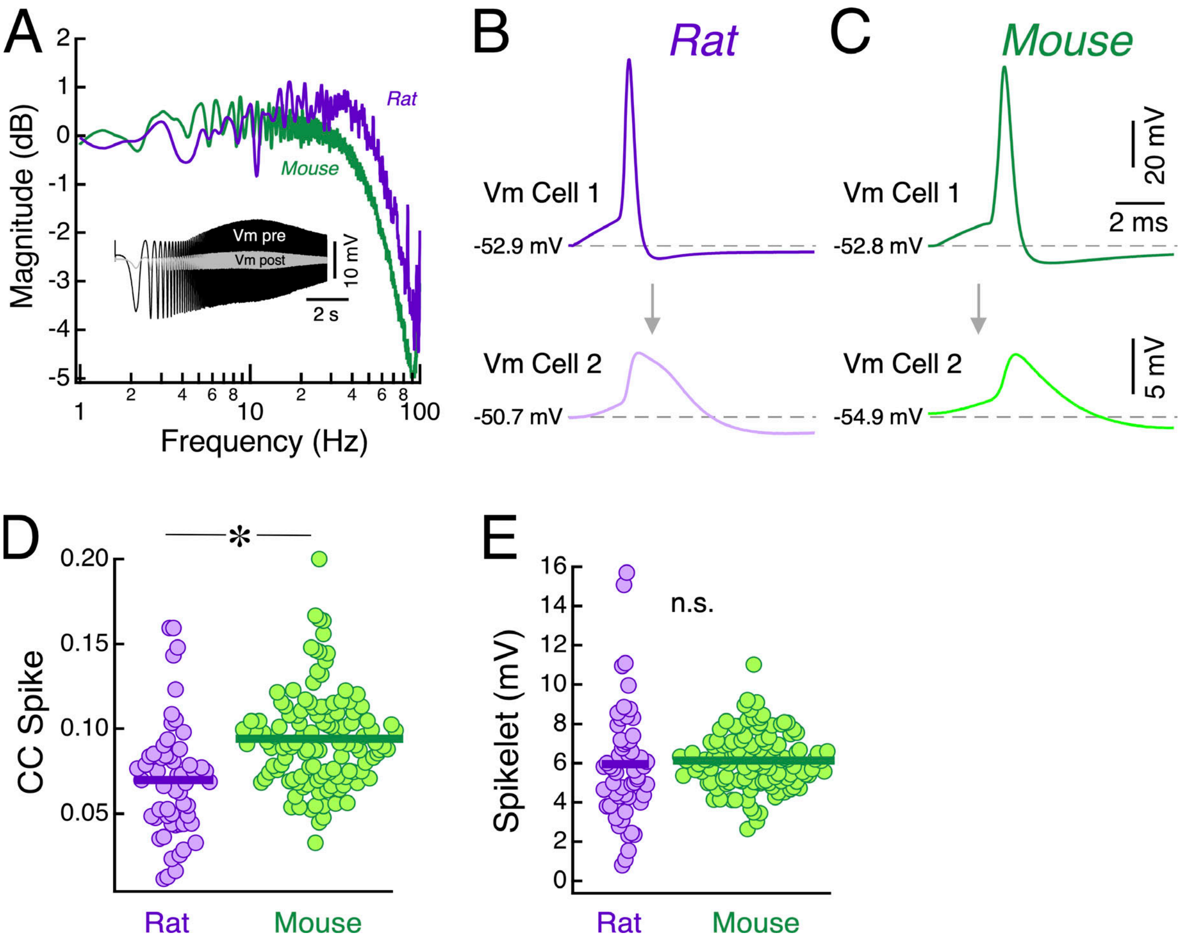

Figure 4. **Spike transmission properties between coupled MesV neurons. (A)** Magnitude of frequency–transfer function between MesV neurons from rats and mice. Each curve represents an average of 14 directions in rats and 34 directions in mice. Inset: Representative membrane responses to ZAP protocols of the pre- and postsynaptic neurons, from which the FFT were determined. **(B and C)** Spike transmission in rats and mice, respectively, showing the presynaptic spike (above, Vm Cell 1) evoked by a short depolarizing current pulse and corresponding coupling potentials in the postsynaptic neurons (below, Vm Cell 2). **(D)** Spike-related coupling coefficient (CC Spike) for the population of assessed directions in rats and mice calculated from recordings like those depicted in B and C (rat: 0.070 ± 0.034 [SD], *n* = 57 directions, *N* = 28 animals; mouse: 0.094 ± 0.028 [SD], *n* = 122 directions, *N* = 50 animals; P = 7.66 × 10^{-6}, unpaired, two-tailed *t* test). **(E)** Spike evoked coupling potential (Spikelet) amplitudes recorded in rats and mice (rat: 5.95 ± 2.91 mV [SD], *n* = 57 cells, *N* = 28 animals; mouse: 6.13 ± 1.41 mV [SD], *n* = 122 cells, *N* = 50 animals; P = 0.645, unpaired, two-tailed *t* test). Horizontal bars in D and E represent population averages.

whereas Vhalf (rat: −39.2 ± 3.8 mV [SD], *n* = 20 cells, *N* = 5 animals; mouse: −36.3 ± 4.2 mV [SD], *n* = 13 cells, *N* = 5 animals; P = 0.056, unpaired, two-tailed *t* test; Fig. 7 D, middle) and slope at Vhalf (rat: 6.92 ± 2.42 mV [SD], *n* = 20 cells, *N* = 5 animals; mouse: 8.54 ± 2.70 mV [SD], *n* = 13 cells, *N* = 5 animals; P = 0.092, unpaired, two-tailed *t* test; Fig. 7 D, right) did not exhibit statistical difference. These results were confirmed by hierarchical statistical analysis which considers possible clustering of data obtained from the same animal (Fig. S2). A comparison of average activation curves for the population of recorded neurons confirms the higher functional expression of ID in mice (Fig. 7 E). Moreover, its incomplete inactivation determines a large window current of about 50–60% of gmax at membrane voltages between −40 and −30 mV and about 10% close to the RMP in both species (Fig. 7, F and G), supporting the notion that ID contributes to set the Rin and the RMP. This is consistent with a more depolarized threshold and lower excitability of mice MesV neurons (Bekkers and Delaney, 2001; Guan et al., 2007; Higgs and Spain, 2011; Ordemann et al., 2019). On the other hand, the INap, whose involvement has also been established as a critical determinant of MesV neurons' excitability in both species (Wu et al., 2001; Enomoto et al., 2006, 2007), showed no significant difference between rats and mice. Indeed, INap gmax averaged 0.096 ± 0.025 nS/pF [SD], (*n* = 10 cells, *N* = 3 animals) and 0.12 ± 0.075 nS/pF [SD] (*n* = 8 cells, *N* = 4 animals) in rats and mice, respectively (P = 0.445, unpaired, two-tailed *t* test). The Vhalf averaged −45.9 ± 4.5 mV [SD] (*n* = 10 cells, *N* = 3 animals) and −43.2 ± 8.2 mV [SD] (*n* = 8 cells, *N* = 4 animals) in rats and mice, respectively (P = 0.412, unpaired, two-tailed *t* test), whereas the slope at Vhalf averaged 5.1 ± 1.0 mV [SD] (*n* = 10 cells, *N* = 3 animals) and 6.0 ± 2.4 mV [SD] (*n* = 8 cells, *N* = 4 animals) in rats and mice, respectively (P = 0.356, unpaired, two-tailed *t* test; Fig. S3, A–E). These results were confirmed by hierarchical statistical analysis which considers possible clustering of data obtained from the same animal (Fig. S3 F).

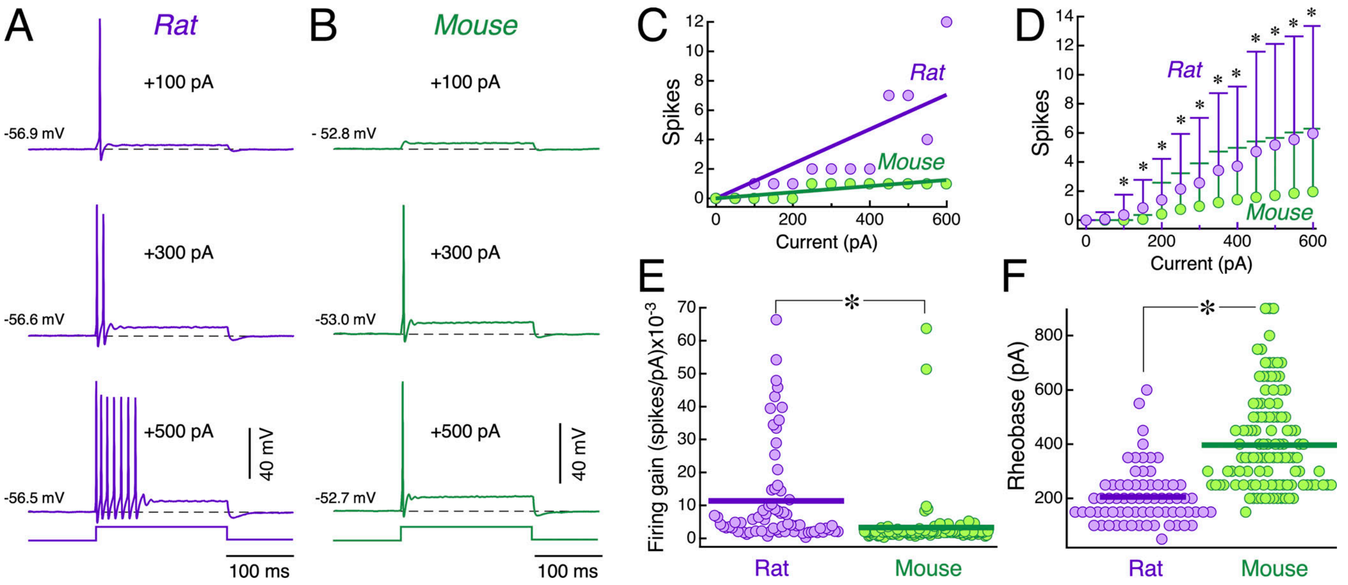

Figure 5. **Firing properties of MesV neurons. (A and B)** Representative responses of a MesV neuron to intracellular depolarizing current pulses of increasing magnitude from rats and mice, respectively. **(C)** Plot of the number of spikes evoked by current pulses of 200 ms in duration as a function of the injected current intensity for the same neurons depicted in A and B. Linear regression fits are shown superimposed to each data set. **(D)** Plot of the mean number of spikes evoked by current pulses (200 ms duration) as a function of the injected current intensity, for the population of recorded MesV neurons from rats (n = 68 cells, N = 29 animals, purple symbols) and mice (n = 99 cells, N = 45 animals, green symbols). Error bars represent SD. For each current intensity, the statistical difference between rats and mice was evaluated by using unpaired, two-tailed t test (0 pA: P = N/A; 50 pA: P = N/A; 100 pA: P = 0.0023; 150 pA: P = 4.8×10^{-5}; 200 pA: P = 0.0302; 250 pA: P = 0.0160; 300 pA: P = 0.0190; 350 pA: P = 0.0058; 400 pA: P = 0.0052; 450 pA: P = 0.0017; 500 pA: P = 0.0006; 550 pA: P = 0.0004; 600 pA: P = 0.0002). **(E)** Slope values of linear regression fitted to spikes vs. current relationships (firing gain) like those depicted in C, for rats (purple symbols) and mice (green symbols; rat: 0.011 ± 0.015 spikes/pA [SD], range: 0.0004–0.0664, n = 70 cells, N = 31 animals; mouse: 0.003 ± 0.008 spikes/pA [SD], range: 0.0004–0.0637, n = 99 cells, N = 50 animals; P = 7.19×10^{-5}, unpaired, two-tailed t test). **(F)** Plot of the rheobase for the population of recorded MesV neurons from rats and mice (rat: 205.7 ± 104.4 pA [SD], n = 70 cells, N = 31 animals; mouse: 396.2 ± 181.4 pA [SD], n = 128 cells, N = 50 animals; P = 1.12×10^{-16}, unpaired, two-tailed t test). Horizontal bars in E and F represent population averages.

Taken together, the preceding results strongly suggest that the higher level of ID expression in MesV neurons from mice underlies their lower excitability in relation to rat MesV neurons. To confirm this interpretation, the involvement of ID in regulating cellular excitability was directly assessed by a pharmacological approach. Fig. 8, A and B, shows results from mice MesV neurons in which the addition of 4-AP (30 µM) to block ID resulted in a marked increase in firing for the entire range of injected current intensity. In fact, these neurons that typically respond to depolarizing current pulses with one or two spikes in control conditions, in the presence of 4-AP, respond with robust repetitive responses. Consistently, the firing gain (slope of linear regressions of spikes vs. current relationships) displayed a significant increase from 0.0015 ± 0.0004 spikes/pA [SD] in control to 0.012 ± 0.010 spikes/pA [SD] after 4-AP addition (n = 19 cells, N = 3 animals; P = 0.00019, paired, two-tailed t test; Fig. 8, B and C), whereas the rheobase was significantly reduced from 389.5 ± 117.4 pA [SD] in control to 78.9 ± 41.9 pA [SD] in the presence of 4-AP (n = 19 cells, N = 3 animals; P = 1.89×10^{-10}, paired, two-tailed t test; Fig. 8 D). In addition, blockade of this membrane conductance resulted in a small but significant depolarization of the RMP (control: −51.7 ± 1.9 mV [SD]; 4-AP: −50.0 ± 3.1 mV [SD]; n = 34 cells, N = 10 animals; P = 0.0010, paired, two-tailed t test), as well as an increase of the Rin (control: 132.9 ± 43.8 MΩ [SD]; 4-AP: 140.1 ± 39.9 MΩ [SD]; n = 34 cells, N = 10 animals; P = 0.0031, paired, two-tailed t test; Fig. S4), thus confirming the involvement of the ID in setting the cell's Rin and RMP as suggested in voltage clamp experiments summarized in Fig. 7 G. These results clearly indicate that the ID plays a critical role regulating membrane excitability, and its expression level contributes to defining the electrophysiological phenotype of MesV neurons in a species-specific fashion. To test whether the control of membrane excitability exerted by ID also has an impact on the efficacy of postsynaptic recruitment, the effect of 4-AP (30 µM) was assessed on the ability of presynaptic action potentials to drive spiking in postsynaptic coupled neurons in mice. Results from these experiments are illustrated in Fig. 8 E, in which spiking in the presynaptic neuron fails to activate the coupled neuron in control conditions (left), whereas after the addition of 4-AP (30 µM), there is a dramatic increase in firing of the postsynaptic cell (right). In fact, while in control conditions recruitment of the postsynaptic neuron was not observed in any of the tested directions, after blockade of the ID, recruitment occurred in 11 out of 19 directions, close to the proportion observed in rats in control conditions (see Fig. 1 C). Consistently, the average number of postsynaptic spikes in relation to presynaptic spikes varied from 0.0 ± 0.0% [SD] in control to 19.7 ± 30.4% [SD] in 4-AP (n = 19 directions, N = 3 animals; P = 0.011, paired, two-tailed t test; Fig. 8 E, inset). These results clearly indicate a critical role of the ID in controlling the efficacy of postsynaptic recruitment, and hence in determining the operation mode of electrical synapses between MesV neurons.

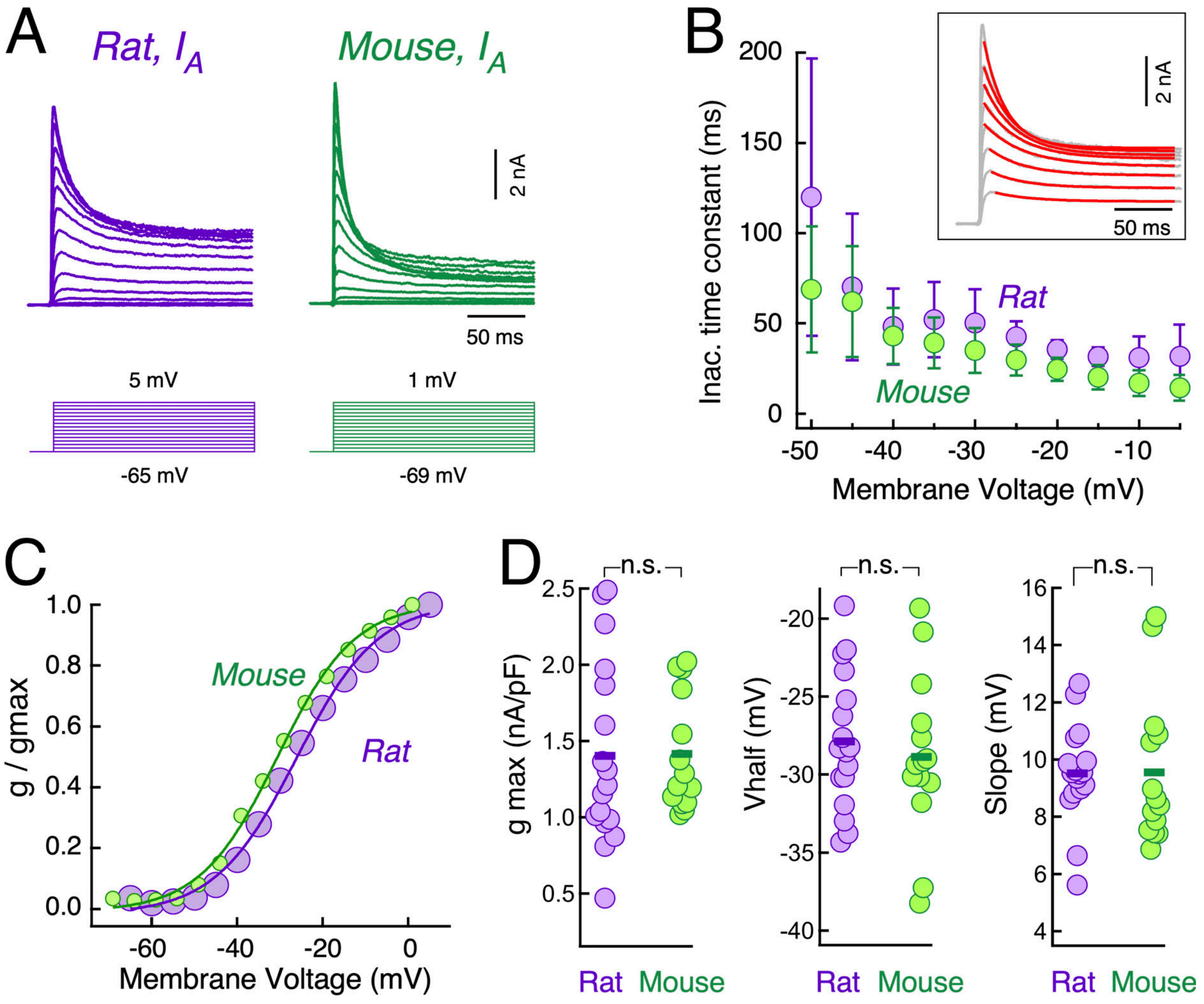

Figure 6. **Characterization of the A-type current of MesV neurons. (A)** Representative traces of IA current of a MesV neuron from rat (left) and mouse (right), obtained by subtracting current traces recorded after the addition of 4-AP (1 mM) from those recorded in the presence of 4-AP (30 μM). Voltage commands employed are illustrated below current traces. **(B)** Plot of inactivation mean time constant as a function of voltage for the population of recorded MesV neurons from rats (n = 13 cells, N = 4 animals, purple symbols) and mice (n = 11 cells, N = 5 animals, green symbols). Error bars represent SD. Inset: fittings to single exponential functions (red traces) to the falling phase of membrane currents during voltage commands (grey traces) to estimate the inactivation time constants. **(C)** Activation curves constructed from traces shown in A. Conductance is normalized by its maximum value. Fits to a Boltzmann function (continuous trace) are superimposed to the experimental data (round symbols). **(D)** Plots of the IA maximal conductance normalized by the cell's capacitance (gmax, left; rat: 1.40 ± 0.61 nS/pF [SD], n = 17 cells, N = 5 animals; mouse: 1.42 ± 0.38 nS/pF [SD], n = 14 cells, N = 6 animals; P = 0.944, unpaired, two-tailed t test), half activation voltage (Vhalf, middle; rat: −27.9 ± 4.4 mV [SD], n = 17 cells, N = 5 animals; mouse: −28.9 ± 5.2 mV [SD], n = 14 cells, N = 6 animals; P = 0.571, unpaired, two-tailed t test) and slope values at Vhalf (Slope, right; rat: 9.51 ± 1.71 mV [SD], n = 17 cells, N = 5 animals; mouse: 9.55 ± 2.61 mV [SD], n = 14 cells, N = 6 animals; P = 0.969, unpaired, two-tailed t test) obtained from fits to Boltzmann function, for the population of recorded neurons. Horizontal bars represent population averages.

Further insights into the mechanism by which such control is exerted was obtained by comparing the spikelets from these two species. Typical examples from rats and mice are illustrated in Fig. 9, A and B, respectively. Despite similar peak amplitudes, their waveforms present important differences. Rat spikelets display a falling phase characterized by large variability and delayed time to peak, resulting in a significant longer duration (Fig. 9 C). Indeed, spikelet half-amplitude duration averaged 4.6 ± 1.8 ms [SD] (n = 22 cells, N = 13 animals) and 2.4 ± 0.7 ms [SD] (n = 106 cells, N = 47 animals) in rats and mice, respectively (P = 2.03×10^{-5}, unpaired, two-tailed t test; Fig. 9 D; see also Table S1). This protracted duration is consistent with the participation of the INap, whose activation promotes the spiking of the postsynaptic coupled neurons in rats (Curti and Pereda, 2004; Curti et al., 2012). In contrast, in mice MesV neurons, which on average express 63% more ID, the INap is strongly antagonized by the swift activation of this outward current, curtailing the spikelets' duration and therefore reducing the efficacy of postsynaptic recruitment. Consistently, blockade of the ID in mice significantly increased the spikelets' time course, whose half-amplitude duration averaged 2.5 ± 0.8 ms [SD] and 4.9 ± 1.4 ms [SD] before and after the addition of 4-AP (30 μM), respectively (P = 2.30×10^{-9}, paired, two-tailed t test; n = 19 cells, N = 6 animals; Fig. 9 E). Noteworthy, this change resulted from the slowing of the spikelet's falling phase (Fig. 9 E, inset). While this approach to assess spike transmission in current clamp

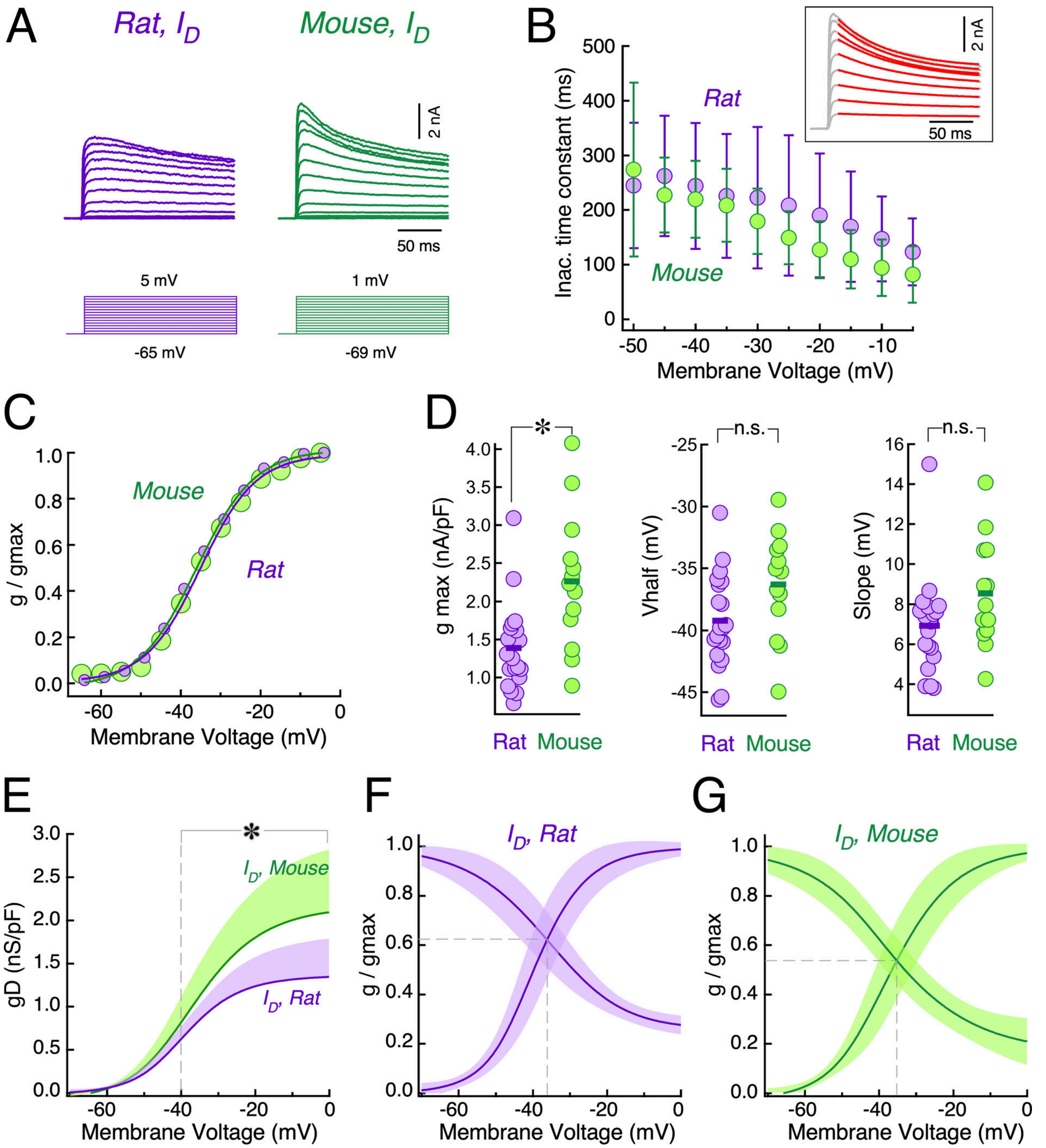

Figure 7. **Characterization of the D-type current of MesV neurons. (A)** Representative traces of ID current of a MesV neuron from rat (left) and mouse (right), obtained subtracting current traces recorded after the addition of 4-AP (30 µM) from those recorded in control. Voltage commands employed are illustrated below current traces. **(B)** Plot of inactivation mean time constant as a function of voltage for the population of recorded MesV neurons from rats (*n* = 14 cells, *N* = 4 animals, purple symbols) and mice (*n* = 10, *N* = 5 animals, green symbols). Error bars represent SD. Inset: Fittings to single exponential functions (red traces) to the falling phase of membrane currents during voltage commands (grey traces) to estimate the inactivation time constants. **(C)** Activation curves constructed from traces shown in A. Conductance is normalized by its maximum value. Fits to Boltzmann function (continuous traces) are superimposed to the experimental data (round symbols). **(D)** Plots of the ID maximal conductance (gmax, left; rat: 1.39 ± 0.56 nS/pF [SD], *n* = 20 cells, *N* = 5 animals; mouse: 2.26 ± 0.90 nS/pF [SD], *n* = 13 cells, *N* = 5 animals; P = 0.0057, unpaired, two-tailed *t* test), half activation voltage (Vhalf, middle; rat: −39.2 ± 3.8 mV [SD], *n* = 20 cells, *N* = 5 animals; mouse: −36.3 ± 4.2 mV [SD], *n* = 13 cells, *N* = 5 animals; P = 0.056, unpaired, two-tailed *t* test) and slope values at Vhalf (Slope, right; rat: 6.92 ± 2.42 mV [SD], *n* = 20 cells, *N* = 5 animals; mouse: 8.54 ± 2.70 mV [SD], *n* = 13 cells, *N* = 5 animals; P = 0.092, unpaired, two-tailed *t* test) obtained from fits to Boltzmann function, for the population of recorded neurons. Horizontal bars represent population averages. **(E)** Plot shows the average activation curves of the ID for the population of recorded neurons in rats (purple; *n* = 20 cells, *N* = 5 animals) and mice (green; *n* = 13 cells, *N* = 5 animals). Conductance values were normalized by the cell's capacitance. Shaded area represents SD. **(F and G)** Activation and inactivation curves of the ID current from rats and mice respectively. Each curve represents the average of fits to Boltzmann function for the population of recorded neurons normalized by its maximum values (rat: *n* = 20 cells, *N* = 5 animals; mouse: *n* = 13 cells, *N* = 5 animals). Shaded area represents SD. Vertical dashed line indicates the intersection between activation and inactivation curves corresponding to the maximum "window" current.

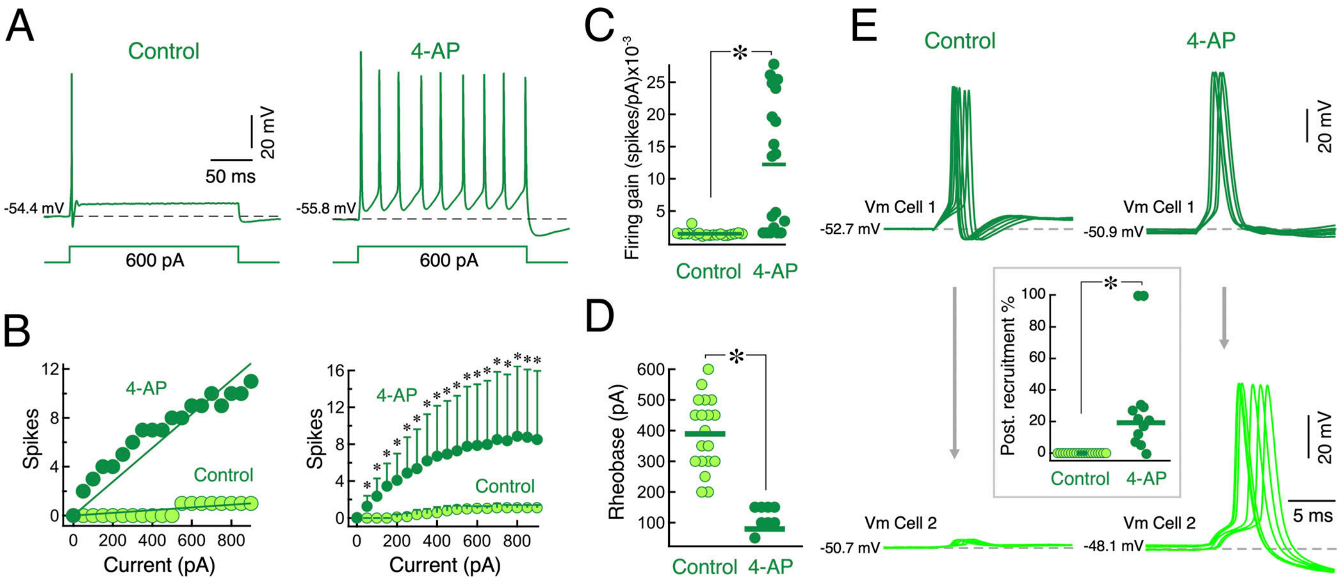

Figure 8. **Blocking ID increases excitability and efficacy of postsynaptic recruitment in mice. (A)** Typical response of a MesV neuron from a mouse to a suprathreshold depolarizing pulse in control conditions (left), and after the addition of 4-AP (30 µM) to the bath solution (right) to block ID current. Below voltage traces are depicted the injected current pulses. **(B)** Plots of the number of spikes evoked by current pulses of 200 ms in duration as a function of the injected current intensity for the same neuron depicted in A (left) and for the population of recorded MesV neurons in mice, in control conditions (light green symbols) and in the presence of 4-AP (30 µM; dark green symbols). Error bars represent SD. For each current intensity, the statistical difference between rats and mice was evaluated by using paired, two-tailed *t* test (0 pA: P = N/A; 50 pA: P = 0.0002; 100 pA: P = 7.7 × 10^{-5}; 150 pA: P = 1.6 × 10^{-5}; 200 pA: P = 1.1 × 10^{-5}; 250 pA: P = 3.5 × 10^{-5}; 300 pA: P = 5.5 × 10^{-5}; 350 pA: P = 7.7 × 10^{-5}; 400 pA: P = 8.5 × 10^{-5}; 450 pA: P = 0.0002; 500 pA: P = 0.0002; 550 pA: P = 0.0003; 600 pA: P = 0.0003; 650 pA: P = 0.0004; 700 pA: P = 0.0004; 750 pA: P = 0.0004; 800 pA: P = 0.0004; 850 pA: P = 0.0003; 900 pA: P = 0.0005; *n* = 19 cells, *N* = 3 animals). **(C)** Firing gain obtained from linear regressions to spikes vs. current relationships as depicted in B at left, in control conditions (light green symbols) and in the presence of 4-AP (30 µM; dark green symbols; control: 0.0015 ± 0.0004 spikes/pA [SD]; 4-AP: 0.012 ± 0.010 spikes/pA [SD], *n* = 19 cells, *N* = 3 animals; P = 0.00019, paired, two-tailed *t* test). **(D)** Rheobase of MesV neurons from mice in control conditions (light green symbols) and in the presence of 4-AP (30 µM; dark green symbols; control: 389.5 ± 117.4 pA [SD]; 4-AP: 78.9 ± 41.9 pA [SD], *n* = 19 cells, *N* = 3 animals; P = 1.89 × 10^{-10}, paired, two-tailed *t* test). **(E)** Representative results obtained in a pair of electrically coupled MesV neurons in which the presynaptic neuron was activated with a short depolarizing current pulse (Vm Cell 1), while recording the corresponding membrane voltage response in the postsynaptic coupled neuron (Vm Cell 2), in control conditions (left) and in the presence of 4-AP (30 µM; right). Six single traces are shown superimposed in order to evaluate the incidence of spiking in the postsynaptic coupled neuron. Inset: Plot of the efficacy of postsynaptic recruitment quantified as the fraction of postsynaptic spikes in relation to presynaptic spikes expressed as a percentage in control conditions (light green symbols) and in the presence of 4-AP (30 µM; dark green symbols; control: 0.0 ± 0.0% [SD]; 4-AP: 19.7 ± 30.4% [SD], *n* = 19 directions, *N* = 3 animals; P = 0.011, paired, two-tailed *t* test).

during paired recordings suggest the involvement of the ID in shaping spikelets, the fact that ID also contributes to spike repolarization (Fig. 8 E; Mitterdorfer and Bean, 2002) implies that changes in presynaptic spike waveform would also affect spikelet duration. Thus, to confirm the involvement of the ID in spike transmission, artificial spikelets were generated in single MesV neurons from mice by injecting current waveforms corresponding to postjunctional currents measured in voltage clamp during paired recordings. For this, pairs of electrically coupled MesV neurons were simultaneously recorded, one cell in current clamp and the other in voltage clamp. While spiking was induced in the current-clamped cell by means of short depolarizing current pulses, the resultant membrane current (postjunctional current) was recorded in the postsynaptic voltage-clamped neuron. During independent recordings from single cells, the opposite (sign reversed) of the postjunctional recorded current was injected as a current clamp command, and its intensity was scaled according to the neuron's Rin to obtain a spikelet of typical amplitude (Fig. 9 F, inset). Such artificial spikelets, which were indistinguishable from real ones (spikelet amplitude: 6.13 ± 1.41 mV [SD], *n* = 122 cells, *N* = 50 animals; artificial spikelet amplitude: 6.63 ± 0.95 [SD], *n* = 17 cells, *N* = 5 animals; P = 0.073, unpaired, two-tailed *t* test), were generated in control conditions and in the presence of 4-AP (30 µM) to evaluate the contribution of the ID to its waveform (Fig. 9 F). In those cases, in which the 4-AP application depolarized the neuron's RMP, it was corrected to near pre-application levels by injecting DC. Confirming our hypothesis, half-amplitude duration of artificial spikelets was significantly increased after ID blockade, averaging 2.0 ± 0.3 ms [SD] and 5.3 ± 5.3 ms [SD] in control and in the presence of 4-AP (30 µM), respectively (P = 0.023, paired, two-tailed *t* test; *n* = 17 cells, *N* = 5 animals). Moreover, recruitment by artificial spikelets increased from 0.0 ± 0.0% [SD] in control to 9.1 ± 16.4% [SD] in the presence of 4-AP (30 µM; P = 0.037, paired, two-tailed *t* test; *n* = 17 cells, *N* = 5 animals). Altogether, these results suggest that the density of ID determines coupling potentials duration and postsynaptic recruitment in electrically coupled MesV neurons.

Discussion

The comparative study of the MesV nucleus from rats and mice exposed a remarkable species-specific difference in the

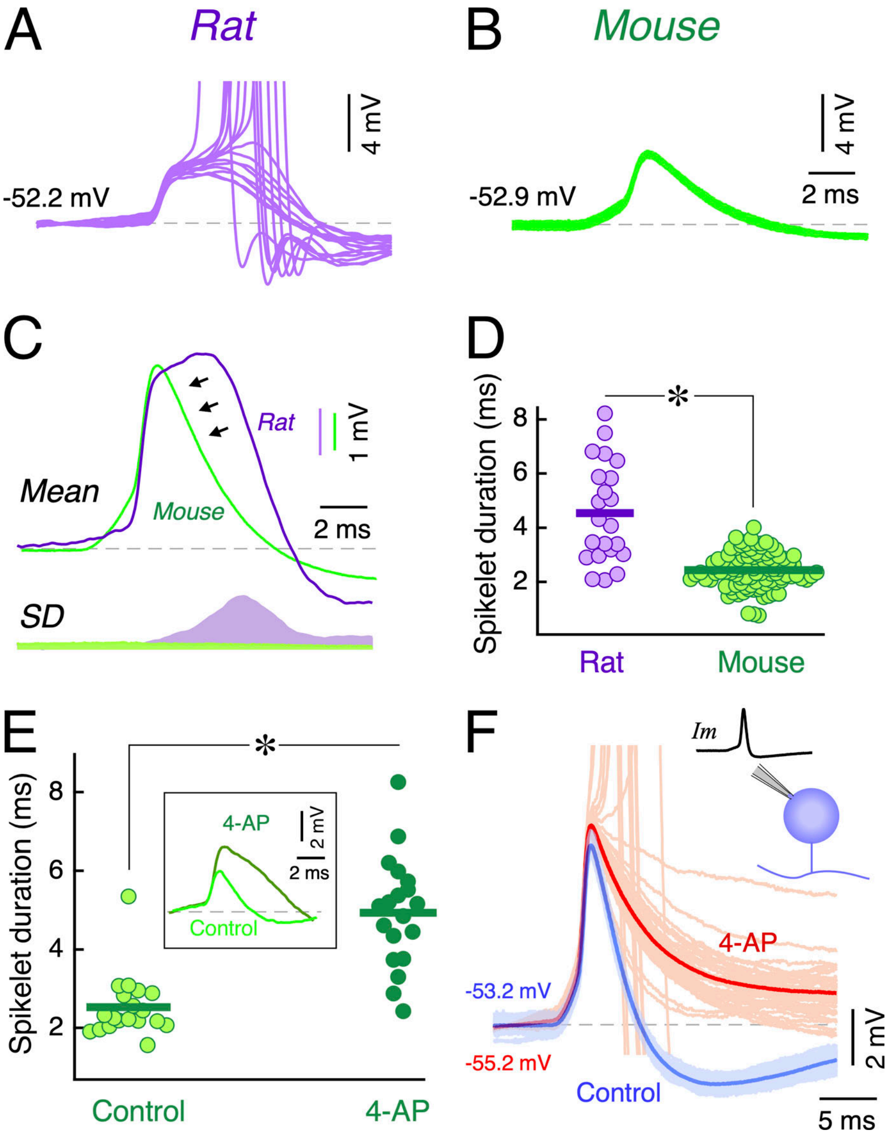

Figure 9. **ID current expression determines spikelet time course. (A and B)** Typical spike-evoked postsynaptic coupling potentials in MesV neurons from rats and mice, respectively. Successive responses are shown superimposed during repetitive activation of the presynaptic neuron. **(C)** Superimposed traces illustrate the averaged postsynaptic potentials (mean, above) and their SD (below) corresponding to the recordings in A and B. Traces with spikes were not included. **(D)** Spikelet half-amplitude duration for rats (4.6 ± 1.8 ms [SD], *n* = 22 cells, *N* = 13 animals; purple symbols) and mice (2.4 ± 0.7 ms [SD], *n* = 106 cells, *N* = 47 animals; green symbols; $P = 2.03 \times 10^{-5}$, unpaired, two-tailed *t* test). **(E)** Spikelet half-amplitude duration for mice in control conditions (2.5 ± 0.8 ms [SD]; light green symbols) and in the presence of 4-AP (30 µM; 4.9 ± 1.4 ms [SD], dark green symbols; $P = 2.30 \times 10^{-9}$, paired, two-tailed *t* test; *n* = 19 cells, *N* = 6 animals). Inset: Representative results showing a spikelet from the mouse before (control) and in the presence of 4-AP (30 µM; 4-AP). Dashed horizontal line indicate pre-spikelet membrane potential (Control: −48.3 mV, 4-AP: −47.3 mV). **(F)** Artificial spikelets in a single mouse MesV neuron evoked by injecting a current waveform corresponding to the junctional current (inset) in control conditions (light blue: single traces; dark blue: average trace) and in the presence of 4-AP (30 µM; light red: single traces; dark red: average trace from single traces without spikes). RMP in the presence of 4-AP was stabilized to a value near control conditions by injecting DC current (−6 pA). Horizontal bars in D and E represent population averages.

operation mode of electrical synapses, revealing the role of the intrinsic electrophysiological properties in shaping the behavior of circuits of coupled neurons. In the present study, a naturally occurring difference in the efficacy of postsynaptic recruitment between electrically coupled MesV neurons was used to uncover the critical role of subthreshold K⁺ currents. We showed that while in rats the spiking of one MesV neuron activates its coupled partner in ∼50% of the cases, this rarely occurs between mice MesV neurons, in which spiking results in a subthreshold postsynaptic response in ∼98% of the tested pairs. Noteworthy, the population of connected MesV neurons from both species bears similar strength of electrical coupling as a result of the comparable magnitude of its determinants (Gj and neuronal Rin). Thus, despite spike-evoked postjunctional coupling potentials (spikelets) from both species being of similar amplitude and arising from a comparable resting membrane potential level, postsynaptic recruitment is considerably more efficient in rats than in mice. This striking difference is imposed by the differential expression of the D-type K⁺ current, whose density is significantly higher in MesV neurons from mice compared with rats. Consistently, previous reports suggested that the firing properties of MesV neurons result from the relative expression of the INap and the subthreshold K⁺ currents (Wu et al., 2001, 2005; Hsiao et al., 2009). With regard to this, MesV neurons have been shown to express several types of Kv1 subunits whose pharmacological profile and voltage dependency match those of the ID characterized in the present study. In fact, α-DTX, considered a specific blocker of Kv1 mediated currents, shows an almost complete overlap in the blocking effect with 4-AP in the low micromolar range (50 µM; Saito et al., 2006; Hsiao et al., 2009). Moreover, while membrane capacitance estimates indicate that MesV neurons from rats present a larger membrane surface area, Rin is similar in both species. This suggests that cells' size difference, which should result in lower Rin values in rats compared with mice, may be compensated by the higher expression level of ID in mice.

A previous experimental and theoretical work has already shown the relevance of active membrane properties levering the activity of networks of coupled neurons, particularly through the action of boosting mechanisms like the INap (Mann-Metzer and Yarom, 1999; Pfeuty et al., 2003; Curti and Pereda, 2004; Dugué et al., 2009; Curti et al., 2012). The synergic operation of these mechanisms endows neural circuits with the ability to generate synchronous and rhythmic patterns of activity with potential functional relevance for both physiological and pathophysiological processes (Draguhn et al., 1998; Perez Velazquez and Carlen, 2000; Hormuzdi et al., 2001; Mylvaganam et al., 2014). Moreover, other circuit operations supported by electrical synapses like coincidence detection are also critically shaped by the intrinsic excitability of neurons. Indeed, the ability of coupled neurons to discriminate between synchronous and temporally uncorrelated inputs is strongly regulated by the hyperpolarization-activated cationic current (H-current; Davoine and Curti, 2019). In spite of this background, direct experimental evidence for the role of K^+ currents in the context of electrical synaptic transmission was lacking. Here, we show that the expression level of the D-type K^+ current, a depolarization-activated subthreshold conductance, whose activation kinetics ranges in the time scale of physiologically relevant signals like action potentials, gates the transfer of spikes between coupled neurons. In fact, the swift activation of this outward current near the resting membrane potential opposes depolarizations, curtailing the duration of spike-evoked coupling potentials and regulating membrane excitability. While the age of the rats and mice employed in this study does not match exactly (rats ranged from P7 to P16, mean: P12.1 d; mice ranged from P12 to P18, mean: P15.1 d), this cannot explain the observed differences. Remarkably, since the excitability of MesV neurons is developmentally regulated (increases) over the first 10 postnatal days (Curti et al., 2012), the opposite findings would be expected in firing properties and efficacy of postsynaptic recruitment if solely based on the age difference between rats and mice. This strongly suggests that our results truly represent phenotypic differences between these species' MesV neurons.

Previous work has shown that the synergistic interaction between electrical coupling and the intrinsic neuronal properties promotes the strong synchronous activation of MesV neurons (Curti et al., 2012). Interestingly, while the efficacy of postsynaptic recruitment in rats is high, facilitating the spread of excitation among MesV neurons, the incidence of electrical coupling is relatively low (∼23% of apposed pairs are electrically coupled in rats compared to ∼63% in mice; Curti et al., 2012). Thus, cellular excitability and electrical coupling at the MesV nucleus of these species are inversely related, suggesting that the expression of these mechanisms is reciprocally regulated in a sort of homeostatic relationship. In this regard, regulations at the network level that reciprocally operates on the expression of mechanisms underlying cellular excitability and interneuronal connectivity supported by gap junctions might be critical to ensure network function stability, as was proposed in networks of neurons interconnected by chemical contacts (Marder and Goaillard, 2006). Indeed, widespread coupling between highly excitable neurons might lead to hypersynchrony and aberrant spiking across neuronal ensembles, characteristic of diseases like epilepsy (Perez Velazquez and Carlen, 2000).

MesV neurons are primary sensory afferents that originate in the spindles of jaw-closing muscles (masseter) and mechanoreceptors of periodontal ligaments (Corbin and Harrison, 1940). In turn, similar to their spinal cord counterparts, MesV neurons establish monosynaptic excitatory connections with motoneurons controlling the same muscles, contributing to the organization of orofacial behaviors (Luo and Li, 1991; Grimwood et al., 1992; Luo et al., 2001; Stanek et al., 2014). Interestingly, differences in the efficacy of postsynaptic recruitment between rats and mice strongly suggest that circuits of electrically coupled MesV neurons from these species operate in totally different regimes. In a large proportion of electrically coupled pairs from rats, activation of one afferent might lead to the activation of a coupled partner, increasing the number of active afferents that respond coordinately to the sensory input, thus supporting lateral excitation as was shown in many sensory systems (El Manira et al., 1993; Herberholz et al., 2002; Rela and Szczupak, 2004). In this way, this phenomenon enhances or amplifies the influence of sensory input on jaw-closing motoneurons. In striking contrast, spike transmission at MesV contacts in mice rarely results in the activation of the postsynaptic neuron due to the higher expression level of the ID, indicating that these contacts do not support lateral excitation. Instead, as these afferents also receive excitatory synaptic input from hierarchical superior centers (Lazarov, 2002), electrical synapses might promote activation of coupled MesV neurons when inputs are temporally correlated, thus acting as coincidence detectors (Davoine and Curti, 2019).

Finally, these findings illustrate how related species display different cellular and circuital strategies to solve the same biological problem, in this case, the control of orofacial behaviors. Similar diversity in homolog circuits from rats and mice has also been shown in hypothalamic neurons controlling pituitary prolactin secretion whose networks display contrasting behaviors. However, in contrast to our findings, such diversity arises from interspecific differences in the electrical coupling, while neurons from both species present comparable membrane properties (Stagkourakis et al., 2018).

Data availability

The data underlying all figures are available in the published article and its online supplemental material.

Acknowledgments

Jeanne M. Nerbonne served as editor.

We thank A. Pereda, G. Budelli, F. Trigo, and V. Abudara for critical discussions and comments.

This work was supported by Agencia Nacional de Investigación e Innovación (ANII), Uruguay (FCE_1_2021_1_166745), Programa de Desarrollo de las Ciencias Básicas (PEDECIBA), and Comisión Académica de Posgrado of Universidad de la República (BDMX_2022_1#48716352).

Author contributions: A. Dapino: Conceptualization, data curation, formal analysis, investigation, methodology, software, visualization, and writing—review & editing. F. Davoine: Conceptualization, data curation, formal analysis, investigation, methodology, software, visualization, and writing—review & editing. S. Curti: Conceptualization, data curation, formal analysis,

funding acquisition, project administration, supervision investigation, methodology, visualization, and writing—original draft.

Disclosures: The authors declare no competing interests exist.

Submitted: 27 January 2023
Revised: 17 May 2023
Accepted: 13 June 2023

References

Alcamí, P., and A.E. Pereda. 2019. Beyond plasticity: The dynamic impact of electrical synapses on neural circuits. *Nat. Rev. Neurosci.* 20:253–271. https://doi.org/10.1038/s41583-019-0133-5

Antonsen, B.L., J. Herberholz, and D.H. Edwards. 2005. The retrograde spread of synaptic potentials and recruitment of presynaptic inputs. *J. Neurosci.* 25:3086–3094. https://doi.org/10.1523/JNEUROSCI.4433-04.2005

Apostolides, P.F., and L.O. Trussell. 2013. Regulation of interneuron excitability by gap junction coupling with principal cells. *Nat. Neurosci.* 16: 1764–1772. https://doi.org/10.1038/nn.3569

Apostolides, P.F., and L.O. Trussell. 2014. Control of interneuron firing by subthreshold synaptic potentials in principal cells of the dorsal cochlear nucleus. *Neuron.* 83:324–330. https://doi.org/10.1016/j.neuron.2014.06.008

Baker, R., and R. Llinás. 1971. Electrotonic coupling between neurones in the rat mesencephalic nucleus. *J. Physiol.* 212:45–63. https://doi.org/10.1113/jphysiol.1971.sp009309

Bekkers, J.M., and A.J. Delaney. 2001. Modulation of excitability by α-dendrotoxin-sensitive potassium channels in neocortical pyramidal neurons. *J. Neurosci.* 21:6553–6560. https://doi.org/10.1523/JNEUROSCI.21-17-06553.2001

Bennett, M.V.L. 1966. Physiology of electrotonic junctions. *Ann. N. Y. Acad. Sci.* 137:509–539. https://doi.org/10.1111/j.1749-6632.1966.tb50178.x

Bennett, M.V. 1997. Gap junctions as electrical synapses. *J. Neurocytol.* 26: 349–366. https://doi.org/10.1023/A:1018560803261

Bennett, M.V.L., and R.S. Zukin. 2004. Electrical coupling and neuronal synchronization in the Mammalian brain. *Neuron.* 41:495–511. https://doi.org/10.1016/S0896-6273(04)00043-1

Stanek, E., IV, S. Cheng, J. Takatoh, B.-X. Han, and F. Wang. 2014. Monosynaptic premotor circuit tracing reveals neural substrates for oro-motor coordination. *Elife.* 3:e02511. https://doi.org/10.7554/eLife.02511

Christie, J.M., and G.L. Westbrook. 2006. Lateral excitation within the olfactory bulb. *J. Neurosci.* 26:2269–2277. https://doi.org/10.1523/JNEUROSCI.4791-05.2006

Connors, B.W. 2017. Synchrony and so much more: Diverse roles for electrical synapses in neural circuits. *Dev. Neurobiol.* 77:610–624. https://doi.org/10.1002/dneu.22493

Connors, B.W., and M.A. Long. 2004. Electrical synapses in the mammalian brain. *Annu. Rev. Neurosci.* 27:393–418. https://doi.org/10.1146/annurev.neuro.26.041002.131128

Corbin, K., and F. Harrison. 1940. Function of mesencephalic root of the fifth cranial nerve. *J. Neurophysiol.* 3:423–435. https://doi.org/10.1152/jn.1940.3.5.423

Curti, S., and J. O'Brien. 2016. Characteristics and plasticity of electrical synaptic transmission. *BMC Cell Biol.* 17:13. https://doi.org/10.1186/s12860-016-0091-y

Curti, S., and A.E. Pereda. 2004. Voltage-dependent enhancement of electrical coupling by a subthreshold sodium current. *J. Neurosci.* 24: 3999–4010. https://doi.org/10.1523/JNEUROSCI.0077-04.2004

Curti, S., G. Hoge, J.I. Nagy, and A.E. Pereda. 2012. Synergy between electrical coupling and membrane properties promotes strong synchronization of neurons of the mesencephalic trigeminal nucleus. *J. Neurosci.* 32: 4341–4359. https://doi.org/10.1523/JNEUROSCI.6216-11.2012

Curti, S., F. Davoine, and A. Dapino. 2022. Function and plasticity of electrical synapses in the mammalian brain: Role of non-junctional mechanisms. *Biology.* 11:81. https://doi.org/10.3390/biology11010081

Davoine, F., and S. Curti. 2019. Response to coincident inputs in electrically coupled primary afferents is heterogeneous and is enhanced by H-current (IH) modulation. *J. Neurophysiol.* 122:151–175. https://doi.org/10.1152/jn.00029.2019

Del Negro, C.A., and S.H. Chandler. 1997. Physiological and theoretical analysis of K$^+$ currents controlling discharge in neonatal rat mesencephalic trigeminal neurons. *J. Neurophysiol.* 77:537–553. https://doi.org/10.1152/jn.1997.77.2.537

Dessem, D., and A. Taylor. 1989. Morphology of jaw-muscle spindle afferents in the rat. *J. Comp. Neurol.* 282:389–403. https://doi.org/10.1002/cne.902820306

Draguhn, A., R.D. Traub, D. Schmitz, and J.G. Jefferys. 1998. Electrical coupling underlies high-frequency oscillations in the hippocampus in vitro. *Nature.* 394:189–192. https://doi.org/10.1038/28184

Dugué, G.P., N. Brunel, V. Hakim, E. Schwartz, M. Chat, M. Lévesque, R. Courtemanche, C. Léna, and S. Dieudonné. 2009. Electrical coupling mediates tunable low-frequency oscillations and resonance in the cerebellar Golgi cell network. *Neuron.* 61:126–139. https://doi.org/10.1016/j.neuron.2008.11.028

Eisner, D.A. 2021. Pseudoreplication in physiology: More means less. *J. Gen. Physiol.* 153:e202012826. https://doi.org/10.1085/jgp.202012826

el Manira, A., D. Cattaert, P. Wallén, R.A. DiCaprio, and F. Clarac. 1993. Electrical coupling of mechanoreceptor afferents in the crayfish: A possible mechanism for enhancement of sensory signal transmission. *J. Neurophysiol.* 69:2248–2251. https://doi.org/10.1152/jn.1993.69.6.2248

Enomoto, A., J.M. Han, C.-F. Hsiao, N. Wu, and S.H. Chandler. 2006. Participation of sodium currents in burst generation and control of membrane excitability in mesencephalic trigeminal neurons. *J. Neurosci.* 26: 3412–3422. https://doi.org/10.1523/JNEUROSCI.5274-05.2006

Enomoto, A., J.M. Han, C.-F. Hsiao, and S.H. Chandler. 2007. Sodium currents in mesencephalic trigeminal neurons from Nav1.6 null mice. *J. Neurophysiol.* 98:710–719. https://doi.org/10.1152/jn.00292.2007

Grimwood, P.D., K. Appenteng, and J.C. Curtis. 1992. Monosynaptic EPSPs elicited by single interneurones and spindle afferents in trigeminal motoneurones of anaesthetized rats. *J. Physiol.* 455:641–662. https://doi.org/10.1113/jphysiol.1992.sp019320

Guan, D., J.C.F. Lee, M.H. Higgs, W.J. Spain, and R.C. Foehring. 2007. Functional roles of Kv1 channels in neocortical pyramidal neurons. *J. Neurophysiol.* 97:1931–1940. https://doi.org/10.1152/jn.00933.2006

Herberholz, J., B.L. Antonsen, and D.H. Edwards. 2002. A lateral excitatory network in the escape circuit of crayfish. *J. Neurosci.* 22:9078–9085. https://doi.org/10.1523/JNEUROSCI.22-20-09078.2002

Higgs, M.H., and W.J. Spain. 2011. Kv1 channels control spike threshold dynamics and spike timing in cortical pyramidal neurones. *J. Physiol.* 589: 5125–5142. https://doi.org/10.1113/jphysiol.2011.216721

Hormuzdi, S.G., I. Pais, F.E.N. LeBeau, S.K. Towers, A. Rozov, E.H. Buhl, M.A. Whittington, and H. Monyer. 2001. Impaired electrical signaling disrupts gamma frequency oscillations in connexin 36-deficient mice. *Neuron.* 31:487–495. https://doi.org/10.1016/S0896-6273(01)00387-7

Hsiao, C.F., G. Kaur, A. Vong, H. Bawa, and S.H. Chandler. 2009. Participation of Kv1 channels in control of membrane excitability and burst generation in mesencephalic V neurons. *J. Neurophysiol.* 101:1407–1418. https://doi.org/10.1152/jn.91053.2008

Lazarov, N.E. 2002. Comparative analysis of the chemical neuroanatomy of the mammalian trigeminal ganglion and mesencephalic trigeminal nucleus. *Prog. Neurobiol.* 66:19–59. https://doi.org/10.1016/S0301-0082(01)00021-1

Liem, R.S., J.C. Copray, and J.D. van Willigen. 1991. Ultrastructure of the rat mesencephalic trigeminal nucleus. *Acta Anat.* 140:112–119. https://doi.org/10.1159/000147045

Luo, P.F., and J.S. Li. 1991. Monosynaptic connections between neurons of trigeminal mesencephalic nucleus and jaw-closing motoneurons in the rat: An intracellular horseradish peroxidase labelling study. *Brain Res.* 559:267–275. https://doi.org/10.1016/0006-8993(91)90011-J

Luo, P., M. Moritani, and D. Dessem. 2001. Jaw-muscle spindle afferent pathways to the trigeminal motor nucleus in the rat. *J. Comp. Neurol.* 435:341–353. https://doi.org/10.1002/cne.1034

Mann-Metzer, P., and Y. Yarom. 1999. Electrotonic coupling interacts with intrinsic properties to generate synchronized activity in cerebellar networks of inhibitory interneurons. *J. Neurosci.* 19:3298–3306. https://doi.org/10.1523/JNEUROSCI.19-09-03298.1999

Marder, E., and J.-M. Goaillard. 2006. Variability, compensation and homeostasis in neuron and network function. *Nat. Rev. Neurosci.* 7: 563–574. https://doi.org/10.1038/nrn1949

Mitterdorfer, J., and B.P. Bean. 2002. Potassium currents during the action potential of hippocampal CA3 neurons. *J. Neurosci.* 22:10106–10115. https://doi.org/10.1523/JNEUROSCI.22-23-10106.2002

Morquette, P., R. Lavoie, M.-D. Fhima, X. Lamoureux, D. Verdier, and A. Kolta. 2012. Generation of the masticatory central pattern and its modulation by sensory feedback. *Prog. Neurobiol.* 96:340–355. https://doi.org/10.1016/j.pneurobio.2012.01.011

Mylvaganam, S., M. Ramani, M. Krawczyk, and P.L. Carlen. 2014. Roles of gap junctions, connexins, and pannexins in epilepsy. *Front. Physiol.* 5:172. https://doi.org/10.3389/fphys.2014.00172

Nagy, J.I., and B.D. Lynn. 2018. Structural and intermolecular associations between Connexin36 and protein components of the adherens junction-neuronal gap junction complex. *Neuroscience*. 384:241–261. https://doi.org/10.1016/j.neuroscience.2018.05.026

Ordemann, G.J., C.J. Apgar, and D.H. Brager. 2019. D-type potassium channels normalize action potential firing between dorsal and ventral CA1 neurons of the mouse hippocampus. *J. Neurophysiol.* 121:983–995. https://doi.org/10.1152/jn.00737.2018

Pereda, A.E., T.D. Bell, and D.S. Faber. 1995. Retrograde synaptic communication via gap junctions coupling auditory afferents to the Mauthner cell. *J. Neurosci.* 15:5943–5955. https://doi.org/10.1523/JNEUROSCI.15-09-05943.1995

Pereda, A.E., S. Curti, G. Hoge, R. Cachope, C.E. Flores, and J.E. Rash. 2013. Gap junction-mediated electrical transmission: Regulatory mechanisms and plasticity. *Biochim. Biophys. Acta*. 1828:134–146. https://doi.org/10.1016/j.bbamem.2012.05.026

Perez Velazquez, J.L., and P.L. Carlen. 2000. Gap junctions, synchrony and seizures. *Trends Neurosci.* 23:68–74. https://doi.org/10.1016/S0166-2236(99)01497-6

Pfeuty, B., G. Mato, D. Golomb, and D. Hansel. 2003. Electrical synapses and synchrony: The role of intrinsic currents. *J. Neurosci.* 23:6280–6294. https://doi.org/10.1523/JNEUROSCI.23-15-06280.2003

Rela, L., and L. Szczupak. 2004. Gap junctions: Their importance for the dynamics of neural circuits. *Mol. Neurobiol.* 30:341–357. https://doi.org/10.1385/MN:30:3:341

Saito, M., Y. Murai, H. Sato, Y.-C. Bae, T. Akaike, M. Takada, and Y. Kang. 2006. Two opposing roles of 4-AP-sensitive K^+ current in initiation and invasion of spikes in rat mesencephalic trigeminal neurons. *J. Neurophysiol.* 96:1887–1901. https://doi.org/10.1152/jn.00176.2006

Stagkourakis, S., C.T. Pérez, A. Hellysaz, R. Ammari, and C. Broberger. 2018. Network oscillation rules imposed by species-specific electrical coupling. *Elife*. 7:e33144. https://doi.org/10.7554/eLife.33144

Storm, J.F. 1988. Temporal integration by a slowly inactivating K^+ current in hippocampal neurons. *Nature*. 336:379–381. https://doi.org/10.1038/336379a0

Storm, J.F. 1990. Potassium currents in hippocampal pyramidal cells. *Prog. Brain Res.* 83:161–187. https://doi.org/10.1016/S0079-6123(08)61248-0

Trenholm, S., D.J. Schwab, V. Balasubramanian, and G.B. Awatramani. 2013. Lag normalization in an electrically coupled neural network. *Nat. Neurosci.* 16:154–156. https://doi.org/10.1038/nn.3308

Verdier, D., J.P. Lund, and A. Kolta. 2004. Synaptic inputs to trigeminal primary afferent neurons cause firing and modulate intrinsic oscillatory activity. *J. Neurophysiol.* 92:2444–2455. https://doi.org/10.1152/jn.00279.2004

Vervaeke, K., A. Lorincz, Z. Nusser, and R.A. Silver. 2012. Gap junctions compensate for sublinear dendritic integration in an inhibitory network. *Science*. 335:1624–1628. https://doi.org/10.1126/science.1215101

Weinberg, E. 1928. The mesencephalic root of the fifth nerve. A comparative anatomical study. *J. Comp. Neurol.* 46:249–405. https://doi.org/10.1002/cne.900460202

Wu, N., C.F. Hsiao, and S.H. Chandler. 2001. Membrane resonance and subthreshold membrane oscillations in mesencephalic V neurons: Participants in burst generation. *J. Neurosci.* 21:3729–3739. https://doi.org/10.1523/JNEUROSCI.21-11-03729.2001

Wu, N., A. Enomoto, S. Tanaka, C.-F. Hsiao, D.Q. Nykamp, E. Izhikevich, and S.H. Chandler. 2005. Persistent sodium currents in mesencephalic V neurons participate in burst generation and control of membrane excitability. *J. Neurophysiol.* 93:2710–2722. https://doi.org/10.1152/jn.00636.2004

Yang, J., J.-L. Xing, N.-P. Wu, Y.-H. Liu, C.-Z. Zhang, F. Kuang, V.-Z. Han, and S.-J. Hu. 2009. Membrane current-based mechanisms for excitability transitions in neurons of the rat mesencephalic trigeminal nuclei. *Neuroscience*. 163:799–810. https://doi.org/10.1016/j.neuroscience.2009.07.007

Supplemental material

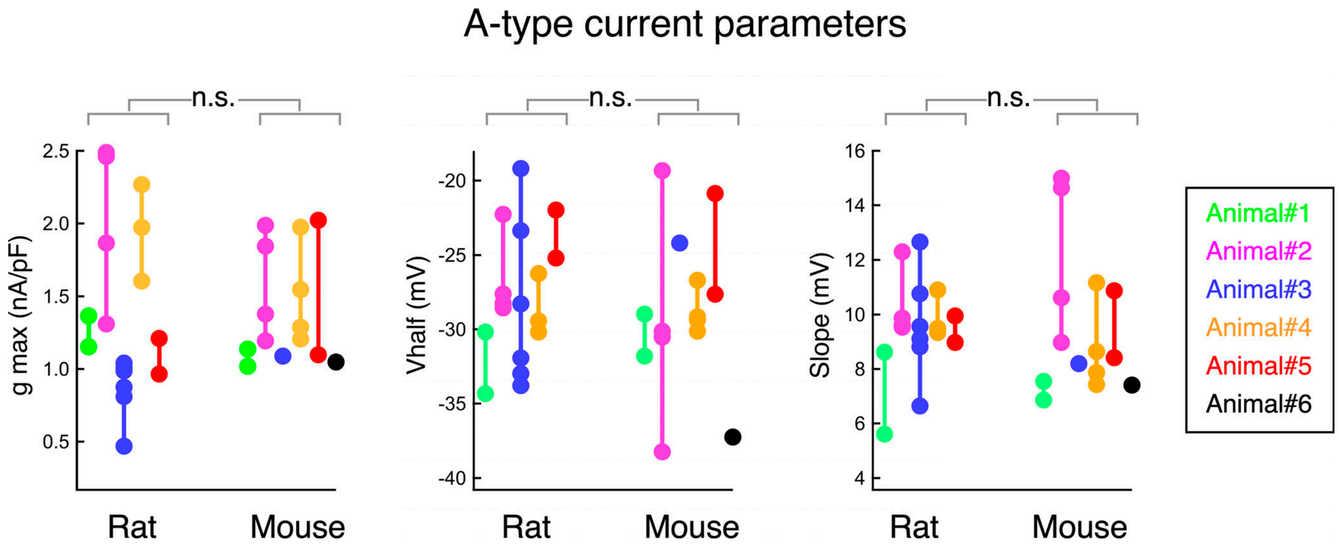

Figure S1. **Assessment of statistical significance by hierarchical analysis of the A-type current of MesV neurons.** To consider possible clustering of data obtained from the same animal, the statistical significance of the parameters obtained from fits to Boltzmann functions for the population of recorded neurons shown in Fig. 6, was reevaluated by unpaired, two-tailed nested Student's *t* test. Results obtained from cells belonging to the same animal are depicted in the same color. Left: Plot of the IA maximal conductance normalized by the cell's capacitance (gmax; rat: *n* = 17 cells, *N* = 5 animals; mouse: *n* = 14 cells, *N* = 6 animals; P = 0.7318, unpaired, two-tailed nested *t* test). Middle: Plot of the half activation voltage (Vhalf; rat: *n* = 17 cells, *N* = 5 animals; mouse: *n* = 14 cells, *N* = 6 animals; P = 0.5637, unpaired, two-tailed nested *t* test). Right: Plot of the slope values at Vhalf (Slope; rat: *n* = 17 cells, *N* = 5 animals; mouse: *n* = 14 cells, *N* = 6 animals; P = 0.8908, unpaired, two-tailed nested *t* test).

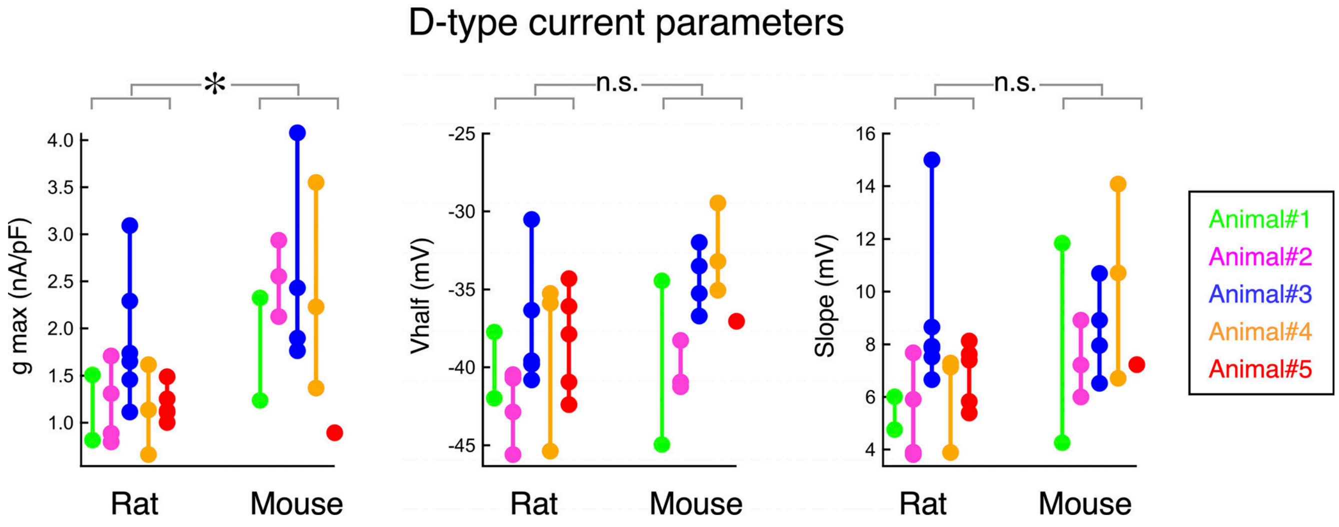

Figure S2. **Assessment of statistical significance by hierarchical analysis of the D-type current of MesV neurons.** To consider possible clustering of data obtained from the same animal, the statistical significance of the parameters obtained from fits to Boltzmann functions for the population of recorded neurons shown in Fig. 7, was reevaluated by unpaired, two-tailed nested Student's *t* test. Results obtained from cells belonging to the same animal are depicted in the same color. Left: Plot of the ID maximal conductance normalized by the cell's capacitance (gmax; rat: *n* = 20 cells, *N* = 5 animals; mouse: *n* = 13 cells, *N* = 5 animals; P = 0.0141, unpaired, two-tailed nested *t* test). Middle: Plot of the half activation voltage (Vhalf; rat: *n* = 20 cells, *N* = 5 animals; mouse: *n* = 13 cells, *N* = 5 animals; P = 0.1448, unpaired, two-tailed nested *t* test). Right: Plot of the slope values at Vhalf (Slope; rat: *n* = 20 cells, *N* = 5 animals; mouse: *n* = 13 cells, *N* = 5 animals; P = 0.1328, unpaired, two-tailed nested *t* test).

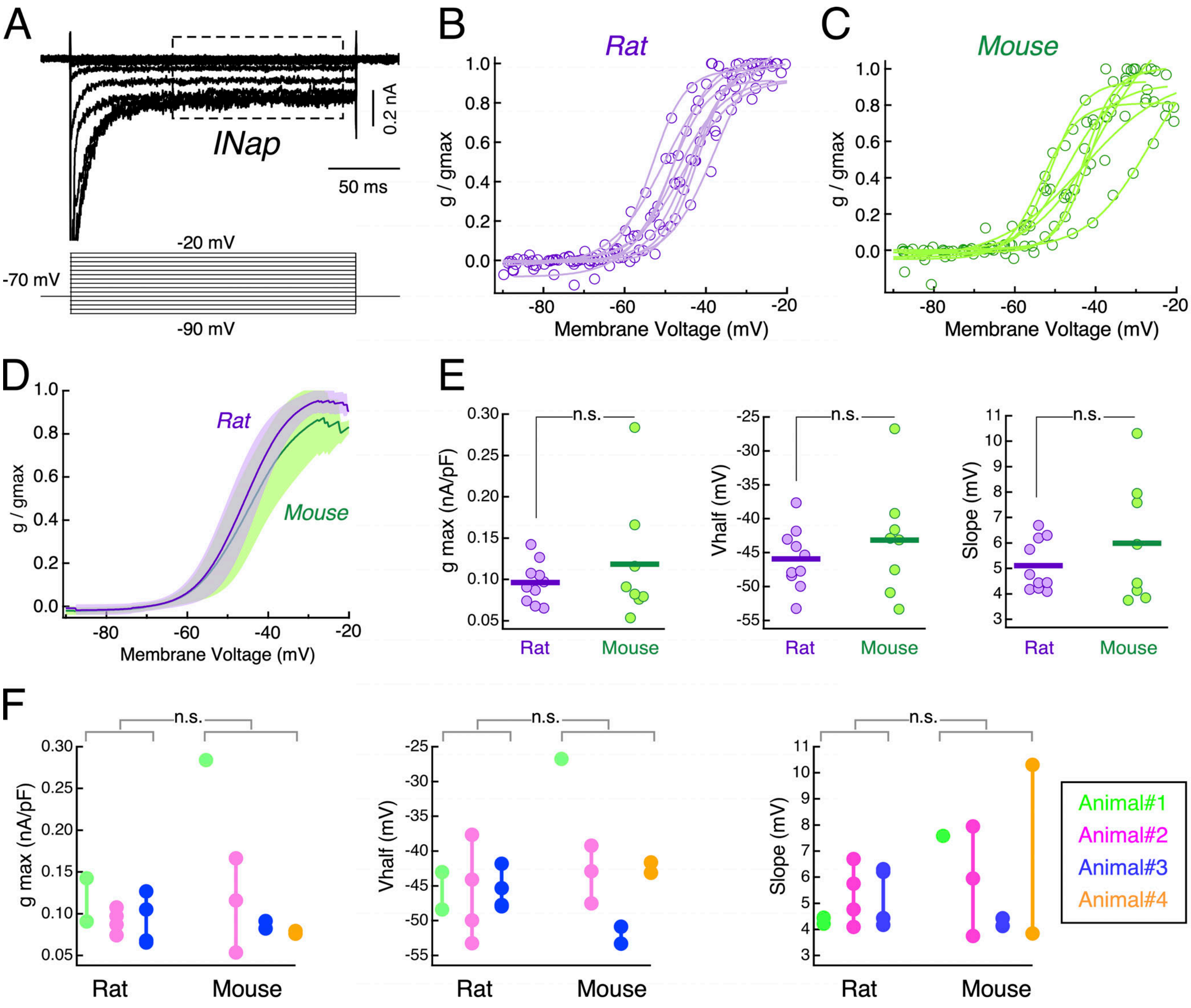

Figure S3. **Characterization of the persistent Na⁺ current of MesV neurons. (A)** Representative traces of the INap obtained by subtracting current traces recorded after the addition of TTX (0.5 µM) from those recorded in control (above), and the voltage commands employed (below). **(B and C)** Activation curves from the population of recorded MesV neurons from rats and mice, respectively (rat: *n* = 10 cells, *N* = 3 animals; mouse: *n* = 8 cells, *N* = 4 animals). Experimental values (round symbols) and fits a Boltzmann function (continuous traces) are shown superimposed. Conductance values determined from the TTX-sensitive and non-inactivating component of membrane currents (boxed area in A), were normalized to maximum values. **(D)** Activation curves of the INap from rats (purple) and mice (green). Each curve represents the average of fits to Boltzmann function for the population of recorded neurons normalized by its maximum values. Shaded area represents SD. **(E)** Plots of the INap maximal conductance, normalized by the cell's capacitance (gmax, left; rat: 0.096 ± 0.025 nS/pF [SD], *n* = 10 cells, *N* = 3 animals; mouse: 0.119 ± 0.075 nS/pF [SD], *n* = 8 cells, *N* = 4 animals; P = 0.4450, unpaired, two-tailed *t* test), half activation voltage (Vhalf, middle; rat: −45.9 ± 4.5 mV [SD], *n* = 10 cells, *N* = 3 animals; mouse: −43.2 ± 8.2 mV [SD], *n* = 8 cells, *N* = 4 animals; P = 0.4118, unpaired, two-tailed *t* test) and slope values at Vhalf (Slope, right; rat: 5.1 ± 1.0 mV [SD], *n* = 10 cells, *N* = 3 animals; mouse: 6.0 ± 2.4 mV [SD], *n* = 8 cells, *N* = 4 animals; P = 0.3560, unpaired, two-tailed *t* test) obtained from fits to Boltzmann function, for the population of recorded neurons. Horizontal bars represent population averages. **(F)** To consider possible clustering of data obtained from the same animal, the statistical significance of the parameters shown in E was re-evaluated by unpaired, two-tailed nested Student's *t* test. Results obtained from cells belonging to the same animal are depicted in the same color. Plots of the INap maximal conductance normalized by the cell's capacitance (gmax, left; rat: *n* = 10 cells, *N* = 3 animals; mouse: *n* = 8 cells, *N* = 4 animals; P = 0.5199, unpaired, two-tailed nested *t* test), half activation voltage (Vhalf, middle; rat: *n* = 10 cells, *N* = 3 animals; mouse: *n* = 8 cells, *N* = 4 animals; P = 0.4829, unpaired, two-tailed nested *t* test), and slope values at Vhalf (Slope, right; rat: *n* = 10 cells, *N* = 3 animals; mouse: *n* = 8 cells, *N* = 4 animals; P = 0.3060, unpaired, two-tailed nested *t* test).

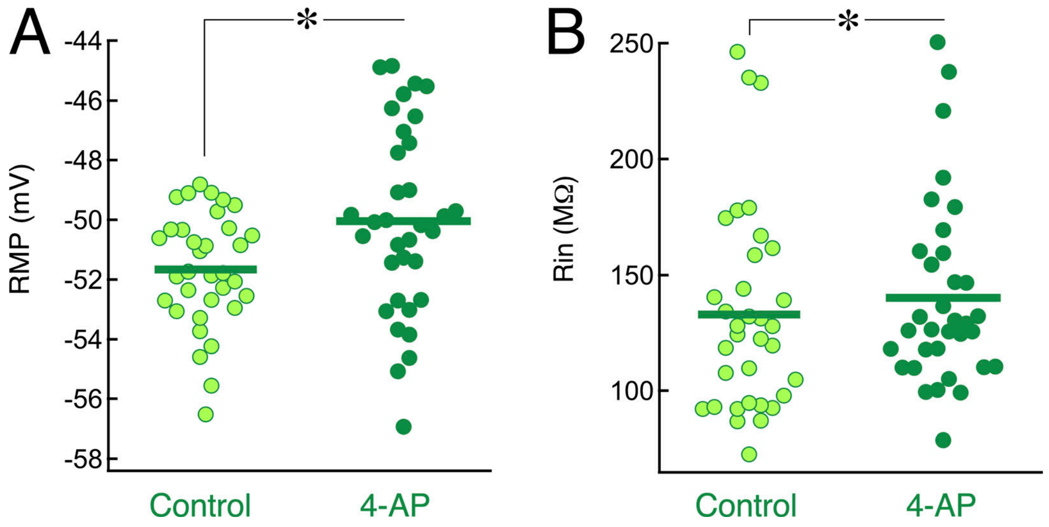

Figure S4. **Contribution of the ID to the RMP and the Rin in mouse MesV neurons. (A)** Resting membrane potential (RMP) measured before (control) and in the presence of 4-AP (30 µM; control: −51.7 ± 1.9 mV [SD]; 4-AP: −50.0 ± 3.1 mV [SD]; *n* = 34 cells, *N* = 10 animals; P = 0.0010, paired, two-tailed *t* test). **(B)** Rin measured before (control) and in the presence of 4-AP (30 µM; control: 132.9 ± 43.8 MΩ [SD]; 4-AP: 140.1 ± 39.9 MΩ [SD]; *n* = 34 cells, *N* = 10 animals; P = 0.0031, paired, two-tailed *t* test). Horizontal bars in A and B represent population averages.

Provided online is Table S1. Table S1 shows statistical analysis related to Figs. 1, 2, 3, 4, 5, and 9.